Research Square

Preprints are preliminary reports that have not undergone peer review.
They should not be considered conclusive, used to inform clinical practice,
or referenced by the media as validated information.

Engineered bacteria as exogenous organelle mimics restore PTEN and p53 tumor suppressor functions for cancer therapy

Jun Liu

jliu1102@ouc.edu.cn

Ocean University of China https://orcid.org/0009-0008-3959-9790

Shijie Bi

Ocean University of China

Maoqin Wang

Shandong University

Qing Guan

Ocean University of China

Yaxin Wang

Ocean University of China

Runchang Liu

Ocean University of China

Jiaying Zhang

Ocean University of China

Meng Li

Ocean University of China

Quan Liu

Ocean University of China

Peng Wang

Ocean University of China

Youming Zhang

Shandong University https://orcid.org/0009-0004-1702-6335

Jun Fu

Shandong University https://orcid.org/0000-0002-5120-4674

Ruijuan Li

Shandong University https://orcid.org/0000-0002-2278-4622

Article

Keywords:

Posted Date: February 25th, 2026

DOI: https://doi.org/10.21203/rs.3.rs-8701444/v1

License: This work is licensed under a Creative Commons Attribution 4.0 International License.
Read Full License

Additional Declarations: There is **NO** Competing Interest.

Abstract

PTEN and p53 are two pivotal tumor suppressor proteins that act synergistically to restrain tumor progression but are frequently inactivated in tumors. Restoration of their tumor suppressor functions holds promise for fundamentally inhibiting tumor growth. However, it is hampered by unsustainable protein production, insufficient intracellular delivery, and off-target side effects. Here, we report a biohybrid therapeutic platform that integrates engineered attenuated *Salmonella typhimurium* VNP20009 (VNP) with nanotechnology to enable durable restoration of PTEN and p53 functions in tumors. The VNP strain was genetically engineered with a quorum-sensing (QS)-regulated lysis and PTEN-expression system, thereby maintaining bacterial density within a controllable range, markedly improving in vivo safety, and enhancing PTEN release by 5.2-fold. Notably, VNP exhibits intrinsic tumor-targeting capability and long-term intracellular parasitism over 7 days, functioning as an exogenous organelle mimic in tumor cells that enables sustained PTEN delivery and restoration of tumor suppressor activity. Moreover, RG7388-loaded nanoparticles (RG-NPs) were conjugated onto the bacterial surface, allowing efficient intracellular delivery and sustained release of an MDM2 inhibitor to elevate p53 levels and synergize with PTEN-mediated tumor suppression. This biohybrid platform achieved up to 94.9% tumor inhibition in a murine melanoma model and conferred long-term survival in 100% of mice when combined with anti-PD-1 therapy, highlighting its strong therapeutic promise for cancer therapy and the potential of engineering VNP as a programmable exogenous organelle mimic.

INTRODUCTION

Tumorigenesis and malignant progression are driven by the combined activation of oncogenes and inactivation of tumor suppressor genes.[1,2] Oncogenic alterations arising from genetic predisposition or environmental insults promote uncontrolled cell growth and proliferation, whereas loss or mutation of tumor suppressors disables critical regulatory mechanisms that restrain malignant transformation.[3,4] As a result, cells fail to repair DNA damage or initiate apoptosis, ultimately leading to unchecked proliferation and tumor formation. Restoring the regulatory mechanisms that govern normal cell growth therefore represents a fundamentally attractive strategy to prevent and treat cancer.

PTEN and p53 are among the most frequently inactivated tumor suppressors in human cancers and play central roles in maintaining cellular homeostasis.[5,6] Cytoplasmic PTEN functions as both a lipid and protein phosphatase, converting phosphatidylinositol (3,4,5)-trisphosphate (PIP3) to phosphatidylinositol (4,5)-bisphosphate (PIP2) and thereby suppressing oncogenic signaling pathways, most notably the PI3K/AKT axis, to inhibit tumor cell growth and proliferation.[7,8] Nuclear PTEN further contributes to tumor suppression by regulating DNA replication and preserving genomic stability.[9] In addition, extracellular PTEN can modulate the tumor immune microenvironment by promoting macrophage polarization toward the pro-inflammatory M1 phenotype, facilitating cytotoxic T cell infiltration, and promoting antitumor immunity.[10,11] Similarly, p53 acts as a master regulator of cell fate by controlling cell-cycle arrest, DNA repair, apoptosis, and senescence.[12] Upon DNA damage, p53 enforces G1/S cell-

cycle arrest to enable repair or, if damage is irreparable, induces apoptosis.[13] Notably, PTEN and p53 engage in reciprocal positive regulation: PTEN stabilizes p53, while p53 transcriptionally upregulates PTEN, resulting in synergistic tumor-suppressive effects.[14,15] Despite their pivotal roles, PTEN and p53 are frequently mutated, deleted, or functionally silenced in tumors, rendering cancer cells refractory to growth control and apoptosis.[16,17] Consequently, restoring intracellular PTEN and p53 functions represents a promising yet highly challenging therapeutic strategy, limited by unsustainable protein production, inefficient intracellular delivery, potential systemic toxicity, and the risk of therapeutic resistance.[18,19]

Bacteria have recently garnered considerable interest as therapeutic agents for cancer owing to several unique advantages.[20–22] Many bacteria species exhibit intrinsic tumor tropism, driven by features of the tumor microenvironment such as hypoxia and slight acidity.[23,24] Moreover, the immunosuppressive nature of tumors facilitates bacterial persistence by limiting immune clearance, thereby enhancing tumor-specific colonization.[25] Bacterial flagella and pili confer motility and tissue penetration capabilities, enabling penetration to the deep tumor core, which is often inaccessible to conventional therapeutics.[26] In addition, bacteria are readily amenable to genetic engineering for the production of macromolecules, including proteins, and can also be functionalized through surface modification or conjugation with small molecules and nanomedicines.[27–30] These attributes position bacteria as potential drug-producing factories and delivery vectors for sustained in situ generation of tumor suppressor proteins, such as PTEN and p53.[31,32] However, inefficient release of expressed proteins and concerns regarding in vivo safety remain major barriers to their clinical translation.[33,34]

In this study, we developed a biohybrid therapeutic platform by integrating engineered bacteria with nanotechnology to recover the dual tumor suppressor functions of PTEN and p53 for cancer therapy. The attenuated *Salmonella typhimurium* strain VNP20009 (VNP), in which the *purI* and *msbB* genes are deleted, was employed that possesses an improved safety profile and enhanced tumor-targeting capability.[35,36] As an intracellular bacterium with a size comparable to cellular organelles and a well-established genetic toolkit, VNP can persist within tumor cells for extended periods, enabling its use as an exogenous, cell-autonomous therapeutic module independent of the host genetic machinery.[37] VNP was first genetically engineered with a quorum-sensing (QS)-regulated lysis and PTEN expression system, enabling density-dependent bacterial lysis and regrowth to maintain the bacterial population within a controllable and safe range.[38] This QS-controlled lysis system markedly reduced potential toxicity associated with uncontrolled bacterial proliferation and promoted sustained release of PTEN proteins in tumor cells, enhancing cytoplasmic PTEN availability and restoring PTEN tumor-suppressive functions. To further synergize PTEN activity with p53 signaling, nanoparticles loaded with the MDM2 inhibitor RG7388 were conjugated onto the bacterial surface. Intracellular parasitism of VNP enabled efficient delivery and sustained release of the MDM2 inhibitor in tumor cells, competitively disrupting the MDM2-p53 interaction, elevating p53 levels, and restoring p53 tumor suppressor functions. This engineered biohybrid platform enables sustained intracellular remodeling of PTEN and p53 signaling,

synergistically induces tumor cell apoptosis and autophagy, and activates antitumor immune responses (Scheme 1). Across multiple murine tumor models, the platform demonstrated potent antitumor efficacy with favorable safety profiles. This work establishes a novel paradigm for using engineered intracellular bacteria as exogenous organelle-like systems to restore tumor suppressor functions and offers a promising strategy for cancer therapy.

RESULTS AND DISCUSSION

Construction and characterization of VPE

To genetically engineer the VNP strain with a quorum-sensing (QS)-regulated PTEN expression system, a *pluxI* promoter-driven lytic gene cassette (*pluxI-LysE*) was integrated into the VNP genome, while a plasmid encoding *pluxI* and PTEN under the control of the *pluxI* promoter was constructed and introduced into VNP cells.[39] During the early growth phase, PTEN and the QS autoinducer acyl-homoserine lactone (AHL) are constitutively expressed and accumulate within the bacterial population. As bacterial density increases and AHL reaches a threshold concentration, AHL binds to LuxR to form the LuxR-AHL complex, which activates the *pluxI* promoter and induces LysE expression.[40] This triggers bacterial lysis and the subsequent release of PTEN into the extracellular environment. Following lysis, the reduction in bacterial density led to decreased AHL levels, preventing LuxR-AHL complex formation and terminating lysis, thereby allowing bacterial regrowth. This negative feedback circuit enabled autonomous regulation of bacterial population density within a therapeutically relevant range (Fig. 1A). Successful genomic integration of the *pluxI-LysE* cassette was verified by agarose gel electrophoresis, which revealed a distinct 739 bp DNA fragment corresponding to the expected size of the insertion at the genomic flanking region (Figs. 1B and S1). Sanger sequencing of the amplified products further confirmed the correct integration, as the observed sequences were identical to the designed construct (**Fig. S2**). To evaluate QS-regulated autonomous lysis, a pBR322-*pluxI*-GFP reporter plasmid was introduced into VPE, enabling GFP expression under QS control. Fluorescence imaging of bacterial colonies revealed a scattered fluorescence pattern in the VPE-GFP group, in contrast to the uniform fluorescence observed in the VNP-GFP control, indicating QS-triggered lysis in VPE (Fig. 1C). Consistently, bacterial growth curves demonstrated that free VNP cells proliferated continuously, reaching an OD600 of approximately 0.57 at 12 h, whereas VPE growth was markedly attenuated, with OD600 values peaking and subsequently declining after 8 h to 0.19 at 12 h, confirming QS-mediated density control (Fig. 1D). Quantification of GFP fluorescence in bacterial suspensions further supported this observation, as total GFP fluorescence in the VPE-GFP group was significantly lower than that in the VNP-GFP group after 7.5 h, likely due to QS-induced LysE-mediated lysis restricting bacterial proliferation (Fig. 1E). To assess protein release following lysis, GFP fluorescence in culture supernatants was measured. Strong fluorescence signals were detected in the supernatant of the VPE-GFP group after 8.5 h, whereas negligible fluorescence was observed in the VNP-GFP group throughout the measurement period (Fig. 1F). This time point coincided with the inflection point of the VPE growth curve, indicating that QS-triggered lysis facilitated GFP release. Quantitative analysis using a microplate reader revealed

that supernatant fluorescence in the VPE-GFP group was approximately 11.3 times higher than that in the VNP-GFP group at 12 h (Fig. 1G). To further investigate intracellular protein release, VPE-GFP and VNP-GFP were co-incubated with 4T1 tumor cells. Fluorescence imaging revealed diffuse cytoplasmic GFP distribution in 4T1 cells treated with VPE-GFP, whereas GFP fluorescence in the VNP-GFP group remained punctate, indicating that GFP was retained within intact bacteria in the absence of QS-mediated lysis (Fig. 1H). Moreover, monitoring of intracellular VNP-GFP following co-culture demonstrated that VNP cells could persist and remain viable within tumor cells for more than 7 days (**Fig. S3**), supporting their suitability as an organelle-mimicking platform for sustained intracellular protein production and release. Collectively, these results demonstrate the successful construction of the QS-controlled lytic bacterial strain VPE, which autonomously regulates bacterial population density to prevent uncontrolled proliferation while enabling efficient release of exogenous synthetic proteins. Furthermore, the prolonged intracellular persistence of VNP highlights its potential as an organelle-like vector for continuous PTEN production within tumor cells.

Verification of PTEN production and safety evaluation of VPE-PTEN

Next, to verify the capability of VPE to produce PTEN, a pBR322-*pluxI*-PTEN plasmid (pPTEN) was constructed and introduced into VPE via electroporation (Fig. 2A). PTEN expression was first confirmed by SDS-PAGE analysis, which revealed a distinct protein band corresponding to the expected molecular weight of PTEN (Fig. 2B). In addition, immunofluorescence imaging staining using a PTEN-specific primary antibody followed by a fluorescently labeled secondary antibody further validated intracellular PTEN expression in VPE cells (**Fig. S4**). Given the QS-regulated autolysis property of VPE, which is expected to facilitate the release of exogenous proteins, PTEN expression and release profiles were further evaluated by western blot analysis. As shown in Fig. 2C, robust PTEN expression was detected in VPE cells following pPTEN electroporation, whereas no PTEN signal was observed in wild-type VNP or VPE strains lacking the pPTEN plasmid. Notably, the PTEN level in the culture supernatant of the VPE-PTEN group was markedly higher than that in the VNP-PTEN group. Quantitative analysis revealed that the extracellular-to-intracellular PTEN ratio in VPE-PTEN was approximately 5.2-fold higher than that in VNP-PTEN (Fig. 2D), indicating that QS-mediated autolysis significantly enhanced PTEN release. These results demonstrate that VPE-PTEN exhibits a substantially improved capacity for extracellular PTEN delivery compared with VNP-PTEN.

Considering that QS-driven autolysis restricts bacterial density and may improve biosafety, the in vivo safety profile of VPE-PTEN was subsequently evaluated. A high bacterial dose (1×10^7 CFU) of either VNP-PTEN or VPE-PTEN was intravenously administered to mice bearing orthotopic 4T1 tumors, and mouse symptoms and survival were monitored (Fig. 2E, i). Within 24 h post-injection, pronounced ecchymosis was observed in mice treated with VNP-PTEN, whereas no obvious abnormalities were detected in the VPE-PTEN group (Fig. 2F), suggesting that QS-controlled bacterial density markedly improved systemic safety. Notably, tumor tissues from the VPE-PTEN group exhibited evident central collapse and necrosis compared with those from the VNP-PTEN group, likely resulting from enhanced

local PTEN release. Survival analysis revealed that all mice receiving VNP-PTEN died within 2 days, whereas only one mouse in the VPE-PTEN group died by day 7, indicating a dramatic improvement in safety (Fig. 2G). To further examine bacterial biodistribution under a tolerable dosing regimen, mice were intravenously injected with 1×10^6 CFU of VNP-PTEN or VPE-PTEN three times, a protocol under which all mice survived (Fig. 2E, **ii**). Biodistribution analysis showed that both strains predominantly accumulated in tumor tissues, confirming the inherent tumor-targeting capability of the VNP platform (Figs. 2H and 2I). However, substantial bacterial presence was still detected in major organs in the VNP-PTEN group, whereas negligible bacterial levels were observed in the VPE-PTEN group, likely due to QS-mediated density limitation and efficient immune clearance of VPE-PTEN. The enhanced tumor specificity of the VPE strain was further validated using VPE-GFP, which exhibited GFP signals selectively localized within tumor tissues (**Fig. S5**). Furthermore, PTEN protein levels in tumor tissues were assessed by western blot. Tumors from the VPE-PTEN group exhibited significantly higher PTEN expression compared with those from the VNP-PTEN group (Fig. 2J), demonstrating the superior PTEN delivery efficiency of the QS-regulated VPE strain at the tumor site. Collectively, these results indicate that VPE-PTEN combines enhanced PTEN production and release with a markedly improved safety profile, characterized by reduced systemic bacterial burden and preferential tumor accumulation. These features highlight VPE-PTEN as a highly promising and controllable bacterial therapeutic agent for anticancer applications.

Evaluation of the in vitro anti-tumor potential of VPE-PTEN

Next, the in vitro antitumor activity of VPE-PTEN was systematically evaluated. Given the established role of PTEN in promoting macrophage polarization toward a pro-inflammatory phenotype, we first assessed the immunomodulatory effects of VPE-PTEN-derived secretions on macrophages. As shown in Figs. 3A and 3B, treatment with 200 μL or 500 μL of concentrated culture supernatant from VPE-PTEN significantly increased the proportion of $F4/80^+CD80^+$ M1-like macrophages to 19.2% and 24.5%, respectively, compared with 12.7% and 17.3% observed by treatment with supernatant from VPE lacking PTEN expression (VPE-WT). These results indicate that secreted PTEN effectively promotes macrophage polarization toward the M1 phenotype. Furthermore, given the tumor-suppressive function of PTEN, the direct antitumor effects of VPE-PTEN were subsequently evaluated by co-incubation with tumor cells (Fig. 3C). MTT assays revealed that VPE-PTEN treatment resulted in significant growth inhibition of both B16F10 and 4T1 cells, with inhibition rates of 46.9% and 39.8%, respectively. In contrast, VPE-WT treatment achieved only modest inhibition (14.9% for B16F10 and 15.9% for 4T1) (Figs. 3D and 3E). Consistent with these findings, morphological examination of 4T1 cells treated with VPE-PTEN showed pronounced cell shrinkage and cytoplasmic vacuolization, hallmark features of apoptosis (Fig. 3F). Additionally, apoptosis induction was further quantified by flow cytometric analysis. As shown in Figs. 3G and 3H, the proportion of apoptotic 4T1 cells in the VPE-PTEN group reached 13.3%, which was markedly higher than that observed in the PBS and VPE-WT control groups. Moreover, considering the role of PTEN in suppressing tumor cell migration, a scratch wound assay was performed to evaluate cell migratory behavior. VPE-PTEN treatment significantly inhibited 4T1 cell migration

compared with both PBS and VPE-WT treatments (Figs. 3I and S6), demonstrating a strong anti-migratory effect.

To elucidate the underlying molecular mechanisms, intracellular PTEN expression and downstream signaling pathways were examined by western blot analysis. As shown in Fig. 3J, VPE-PTEN treatment markedly upregulated PTEN expression and the apoptotic marker cleaved caspase-3, while significantly downregulating phosphorylated AKT (p-AKT), an anti-apoptotic signaling protein. These results confirm that VPE-PTEN restores PTEN signaling and activates apoptosis-related pathways to induce tumor cell death. Furthermore, we investigated whether VPE-PTEN-mediated PTEN restoration could induce autophagy and subsequently enhance dendritic cell (DC) maturation (Fig. 3K). Immunofluorescence analyses revealed a significant upregulation of the autophagy-related protein LC3B following VPE-PTEN treatment (Fig. 3L). Western blot analysis further confirmed increased levels of LC3-I and LC3-II, markers of autophagosome formation (Fig. 3M), indicating robust autophagy induction in tumor cells. Notably, VPE-PTEN-induced autophagy significantly promoted DC maturation, as evidenced by a markedly higher proportion of MHC I^+ DCs (64.7%) in the VPE-PTEN group compared with the PBS (12.6%) and VPE-WT (23.8%) groups (Figs. 3N and 3O). Collectively, these results demonstrate that VPE-PTEN exerts potent antitumor effects in vitro by restoring intracellular PTEN levels, thereby activating apoptotic and autophagic pathways to induce tumor cell death. Simultaneously, VPE-PTEN enhances antitumor immune responses by promoting M1 macrophage polarization and facilitating dendritic cell maturation, underscoring its potential as a multifunctional immuno-oncological therapeutic strategy.

Construction of VPE-PTEN@RG-NPs and evaluation of its antitumor potential

To synergistically integrate the tumor-suppressive functions of PTEN and p53, a biohybrid therapeutic platform was constructed by combining VPE-PTEN with RG7388-loaded nanoparticles (RG-NPs). RG7388 is a potent MDM2 inhibitor that disrupts the MDM2-p53 interaction, thereby stabilizing and upregulating p53 protein levels. For the preparation of RG-NPs, poly(lactic-co-glycolic acid) (PLGA), a biocompatible and biodegradable polymer, was employed to encapsulate RG7388 using a single-emulsion method (Fig. 4A). Transmission electron microscopy (TEM) revealed that RG-NPs exhibited a uniform spherical morphology with good monodispersity (**Fig. S7**). The drug encapsulation efficiency reached 67.4% (**Fig. S8**). Dynamic light scattering analysis showed an average particle size of approximately 182 nm and a zeta potential of -2 mV (Fig. 4B). RG-NPs demonstrated excellent physicochemical stability, with negligible changes in particle size and surface charge after incubation in PBS for over 72 h (**Fig. S9**). Importantly, RG7388 was released from RG-NPs in a sustained and pH-responsive manner, with cumulative release rates of 76.4% at pH 6.5 and 35.9% at pH 7.4 within 48 h (Fig. 4C), indicating preferential drug release under acidic conditions that mimic the tumor microenvironment. Subsequently, RG-NPs were covalently conjugated to the surface of VPE-PTEN to generate VPE-PTEN@RG-NPs. Briefly, carboxyl groups on PLGA were activated using NHS chemistry and subsequently coupled with amine groups on the bacterial surface. TEM imaging confirmed the

successful attachment of RG-NPs onto VPE-PTEN (Fig. 4D). Fluorescence quantification indicated a loading efficiency of up to 77.2% for RG-NPs on the bacterial surface (**Fig. S10**). Notably, RG-NP conjugation did not affect the growth kinetics of VPE-PTEN, suggesting minimal interference with its intrinsic biological characteristics (Fig. 4E).

Following successful construction, the synergistic pro-apoptotic effects of VPE-PTEN@RG-NPs were evaluated in B16F10 and 4T1 tumor cells. As shown in Figs. 4F and 4G, treatment with VPE-PTEN@RG-NPs induced apoptosis in approximately 85.9% of B16F10 cells, which was significantly higher than that observed in all other treatment groups, demonstrating a strong synergistic effect between PTEN and RG7388. The superior apoptotic efficacy of VPE-PTEN@RG-NPs compared with the combination of VPE-PTEN and free RG-NPs is likely attributable to the enhanced intracellular delivery of RG-NPs mediated by the VNP strain, resulting in higher intracellular drug accumulation. Consistently, VPE-PTEN@RG-NPs also exhibited the strongest pro-apoptotic effect in 4T1 cells, with an apoptotic ratio of approximately 60.3% (**Fig. S11**). Propidium iodide (PI) staining further confirmed that VPE-PTEN@RG-NPs induced the highest level of tumor cell death among all groups (Fig. 4H). To elucidate the molecular mechanisms underlying the enhanced antitumor efficacy, PTEN- and p53-related protein expression levels were analyzed by western blotting. As shown in Fig. 4I, VPE-PTEN@RG-NPs treatment markedly increased the expression of PTEN, p53, and the pro-apoptotic marker cleaved caspase-3, confirming effective restoration and activation of tumor-suppressive signaling pathways.

Given the intrinsic tumor-targeting capability of the VNP strain, the efficiency of VPE-PTEN-mediated RG-NP delivery to tumor tissues was further investigated. RG-NPs were fluorescently labeled with DiR, and their biodistribution was monitored using IVIS imaging. As shown in Fig. 4J, DiR-NPs conjugated to VPE-PTEN exhibited significantly enhanced accumulation in tumor tissues compared with free DiR-NPs. Remarkably, strong fluorescence signals persisted in tumors for up to 7 days following VPE-PTEN@DiR-NPs treatment, whereas fluorescence in the DiR-NPs-only group was nearly undetectable. Quantitative analysis revealed that tumor fluorescence intensity in the VPE-PTEN@DiR-NPs group was approximately 1.31-fold higher than that in the DiR-NPs group (Figs. 4K and 4L), indicating improved and sustained nanoparticle retention in tumor tissues. Furthermore, to assess tumor penetration capability, RG-NPs were labeled with FITC and conjugated to VPE-PTEN (VPE-PTEN@FITC-NPs) (**Fig. S12**). Using 3D tumor spheroid models, confocal microscopy revealed that free FITC-NPs were primarily confined to the spheroid periphery, whereas VPE-PTEN@FITC-NPs penetrated deeply into the tumor core after 24 h of incubation (**Fig. S13**). These results demonstrate that VPE-PTEN not only enhances nanoparticle accumulation in tumor tissues but also facilitates deep tumor penetration, thereby maximizing the antitumor efficacy of the delivered therapeutics.

Transcriptomic analysis following VPE-PTEN@RG-NPs treatment

To further elucidate the molecular mechanisms underlying the antitumor efficacy of VPE-PTEN@RG-NPs, transcriptomic profiling of tumor tissues following different treatments was performed. Given the well-established pro-apoptotic functions of PTEN and p53, apoptosis-related gene expression was first

examined. As shown in Fig. 6A, genes encoding pro-apoptotic proteins, including *Fas* and *Casp4*, were significantly upregulated in the VPE-PTEN@RG-NPs group, whereas the expression of anti-apoptotic genes, such as *Bcl2* and *Ddias*, was markedly downregulated. Consistently, compared with the PBS, VPE-WT, and VPE-PTEN + RG-NPs groups, the apoptosis-related gene set was significantly enriched in the VPE-PTEN@RG-NPs group, further confirming the strong apoptosis-inducing capability of this formulation (Figs. 6B, S16A, and S16B). In addition, VPE-PTEN@RG-NPs treatment induced cell-cycle arrest, as evidenced by the downregulation of key cell cycle-associated genes, including *E2f5* and *Cdt1* (**Fig. S16C**).

Beyond apoptosis-related pathways, pronounced differences in immune-related gene expression were observed among the treatment groups. Notably, genes associated with antitumor immune cell activation were broadly upregulated in the VPE-PTEN@RG-NPs group compared with other treatments. These included markers of activated macrophages (*Msr1*, *Marco*, and *Cxcl5*), mature dendritic cells (*Oas3*, *Ido1*, and *Ccl1*), B cells (*Tnfrsf17*, *Cr2*, and *Btk*), and cytotoxic T lymphocytes (*Gzma* and *Prf1*). In contrast, regulatory T cells (Tregs), which contribute to an immunosuppressive tumor microenvironment, were markedly suppressed following VPE-PTEN@RG-NPs treatment, as indicated by reduced *Foxp3* expression (Fig. 6C). Pathway enrichment analysis further revealed that, relative to the PBS group, differentially expressed genes in the VPE-PTEN@RG-NPs group were significantly enriched in immune-related signaling pathways, including the NF-κB and TNF pathways, both of which play central roles in inflammatory and immune regulation. The PI3K-AKT signaling pathway, which is closely associated with tumor cell proliferation and survival, was also prominently enriched, consistent with PTEN-mediated pathway modulation (Fig. 6D). Moreover, Reactome pathway analysis demonstrated that genes upregulated following VPE-PTEN@RG-NPs treatment were significantly enriched in pathways related to immune activation and antitumor responses (Fig. 6E). Overall, these transcriptomic data suggest that VPE-PTEN@RG-NPs exert potent antitumor activity by simultaneously inducing tumor cell apoptosis and reprogramming the tumor immune microenvironment toward a highly immunostimulatory state, providing mechanistic support for their superior therapeutic efficacy in vivo.

VPE-PTEN@RG-NPs induce robust antitumor immune response in vivo

Based on the transcriptomic findings, the immunostimulatory effects of VPE-PTEN@RG-NPs within tumor tissues were further evaluated in vivo. Flow cytometric analysis revealed a pronounced shift in macrophage polarization following VPE-PTEN@RG-NPs treatment, characterized by increased M1-type macrophages ($CD11b^+CD80^+$) and reduced M2-type macrophages ($CD11b^+CD206^+$) compared with all control groups (Fig. 7A). The intratumoral M1/M2 macrophage ratio was markedly elevated in the VPE-PTEN@RG-NPs group, with 1.8-fold, 7.1-fold, 2.2-fold, 6.5-fold, and 17.1-fold higher than those in the VPE-PTEN + RG-NPs, RG-NPs, VPE-PTEN, VPE-WT, and PBS treatment groups, respectively, indicating effective reprogramming toward a pro-inflammatory phenotype (Fig. 7B). Enhanced infiltration of M1 macrophages was further confirmed by confocal microscopy, which showed the strongest CD80-

associated fluorescence in tumors treated with VPE-PTEN@RG-NPs (Fig. 7C). Meanwhile, dendritic cell (DC) maturation was significantly promoted following VPE-PTEN@RG-NPs treatment, as evidenced by increased proportions of mature DCs compared with all other treatment groups (Figs. 7D and 7E). Consistent with improved antigen presentation, cytotoxic $CD8^+$ T cell infiltration within tumor tissues was also markedly increased, with 38.5%, 66.1%, 45.3%, 68.6%, and 84.4% increases compared with the VPE-PTEN + RG-NPs, RG-NPs, VPE-PTEN, VPE-WT, and PBS groups, respectively (Figs. 7F and 7G). These findings were further corroborated by immunofluorescence imaging, which confirmed elevated $CD8^+$ T cell accumulation in tumor tissues (Fig. 7H). In contrast, immunosuppressive regulatory T cells were substantially reduced in the VPE-PTEN@RG-NPs group, indicating effective attenuation of tumor-induced immune suppression (Figs. 7I and 7J). At the molecular level, transcriptomic analysis further supported these immunological findings, revealing significant upregulation of genes involved in antigen presentation (*Nod1*, *Aif1*, and *Ciita*), immune stimulation (*Ctsw*, *Lck*, and *Tbx21*), chemokine signaling (*Cxcl1*, *Ccr1*, and *Ccl3*), and pro-inflammatory cytokine production (*IL-27* and *IL-1α*), following VPE-PTEN@RG-NPs treatment (Fig. 7K). These findings were further validated at the protein level, with ELISA confirming significantly elevated intratumoral levels of TNF-α (Fig. 7L) and IL-1β (Fig. 7M). Overall, these results demonstrate that VPE-PTEN@RG-NPs effectively remodel the tumor immune microenvironment by promoting pro-inflammatory macrophage polarization, enhancing DC maturation, activating cytotoxic T cell responses, and suppressing immunoregulatory pathways, thereby eliciting robust antitumor immunity in vivo.

VPE-PTEN@RG-NPs inhibit the growth and metastasis of 4T1 breast cancer

Next, the therapeutic efficacy of VPE-PTEN@RG-NPs was further evaluated in an orthotopic 4T1 murine breast cancer model. As shown in Fig. 8A, once tumor volume reached approximately 80 ~ 100 mm^3, mice were administered with different formulations intravenously. During the treatment period, negligible mouse body weight loss was observed in all groups, further demonstrating its good safety profile (**Fig. S17**). Moreover, tumor volume was monitored daily. VPE-PTEN@RG-NPs significantly suppressed tumor growth, showing the lowest tumor volumes and smallest tumor weights among all treatment groups (Figs. 8B – 8**E**). Quantitative analysis showed that the tumor inhibitory rate in the VPE-PTEN@RG-NPs group reached 82.6%, significantly higher than the other treatment groups, which showed 57.4%, 33.9%, 50.4%, and 24.3% for VPE-PTEN + RG-NPs, RG-NPs, VPE-PTEN, and VPE-WT, respectively (Fig. 8F). Consistently, the tumor volume doubling time in the VPE-PTEN@RG-NPs group was also the longest among all groups, reaching 11.8 days, 2.2 times that of the PBS group (Fig. 8G). By H&E staining, tumor tissues in the VPE-PTEN@RG-NPs exhibited severe cellular damage, characterized by evident cell lysis and nuclear dissolution (Fig. 8H). Additionally, TUNEL staining demonstrated the highest level of apoptotic cells in tumors treated with VPE-PTEN@RG-NPs treatment, further confirming its potent antitumor efficacy (Fig. 8I).

Enhanced therapeutic efficacy of VPE-PTEN@RG-NPs in combination with anti-PD-1 therapy

The antitumor efficacy of VPE-PTEN@RG-NPs combined with anti-PD-1 (aPD-1) treatment was further investigated in a luciferase-expressing 4T1 breast cancer model (Fig. 9A). No significant body weight loss was observed in any treatment group, including the combination regimen, indicating favorable tolerability (Fig. 9B). Compared with the modest tumor inhibition achieved by aPD-1 monotherapy, VPE-PTEN@RG-NPs alone elicited a pronounced tumor-suppressive effect, as evidenced by a slower increase in tumor volume (Fig. 9C). Notably, the combination of VPE-PTEN@RG-NPs and aPD-1 produced the most robust antitumor response, resulting in the lowest tumor weights and weakest bioluminescence signals among all groups (Fig. 9D). Longitudinal bioluminescence imaging further revealed that, whereas tumor signals progressively increased in the other treatment groups, bioluminescence intensity in the VPE-PTEN@RG-NPs + aPD-1 group continuously declined throughout the treatment period, demonstrating sustained and potent tumor suppression (Fig. 9E). Survival analysis showed that all mice in the PBS and aPD-1 groups died within 24 and 52 days, respectively, whereas VPE-PTEN@RG-NPs monotherapy significantly prolonged survival, with 60% of mice remaining alive over 80 days (Fig. 9F). Strikingly, the combination treatment achieved 100% survival over 80 days, indicating a strong synergistic enhancement of antitumor immunity when VPE-PTEN@RG-NPs were combined with immune checkpoint blockade. Furthermore, to assess whether local therapy could elicit systemic antitumor immunity, a bilateral tumor model was established (Fig. 9G). Intratumoral administration of VPE-PTEN@RG-NPs into the primary tumor markedly suppressed the growth of both primary and distant tumors. By day 21, tumor weights of the primary and distant lesions were reduced by 83.1% and 91.6%, respectively, compared with the PBS group (Fig. 9H-9M). Collectively, these results demonstrate that VPE-PTEN@RG-NPs synergize with aPD-1 therapy to achieve superior antitumor efficacy and that local VPE-PTEN@RG-NPs treatment can induce systemic immune responses capable of inhibiting distant tumor growth and metastasis.

CONCLUSION

Loss or functional inactivation of tumor suppressor proteins is a fundamental driver of tumor initiation and progression,[41] making restoration of their activity an attractive therapeutic strategy.[42,43] Although small-molecule agents can transiently modulate tumor suppressor pathways, their clinical utility is often limited by nonspecific biodistribution, systemic toxicity, and the emergence of drug resistance.[44] Direct administration of tumor suppressor proteins is also challenging because of their instability and poor cellular internalization,[45] while nanoparticle-mediated protein delivery typically results in only short-lived and unsustained intracellular expression.[46]

Here, we report an intracellular, organelle-mimicking therapeutic platform based on the attenuated bacterium Salmonella VNP20009. Owing to its subcellular dimensions and intrinsic tumor tropism, VNP can persist within tumor cells for extended periods (> 7 days), enabling its use as an exogenous

intracellular “organelle.” By genetically engineering VNP to constitutively produce PTEN, we achieved sustained intracellular restoration of PTEN tumor suppressor function. Importantly, a QS-regulated lysis circuit was incorporated to dynamically control bacterial density, triggering lysis at high bacterial loads and regrowth at low density. This self-regulating system enhanced the release of exogenously expressed proteins by more than 5.2-fold while markedly improving in vivo safety. The resulting QS-regulated PTEN-expressing VNP (VPE-PTEN) significantly elevated intratumoral PTEN levels, suppressed AKT signaling, and promoted tumor cell apoptosis. In parallel, released PTEN reprogrammed the tumor immune microenvironment by polarizing macrophages toward a pro-inflammatory M1 phenotype, thereby augmenting antitumor immunity. To further exploit the frequent loss of p53 function in tumors and its synergistic interaction with PTEN, a biohybrid platform was constructed by conjugating MDM2 inhibitor-loaded nanoparticles (RG-NPs) onto the VPE-PTEN surface. Tumor targeting and intracellular parasitism by VNP enabled efficient delivery and sustained release of the MDM2 inhibitor, leading to robust p53 reactivation and synergistic induction of tumor cell apoptosis. Across multiple murine tumor models, VPE-PTEN@RG-NPs achieved > 90% tumor inhibition and, when combined with anti-PD-1 therapy, conferred long-term survival in all treated mice (> 80 days), highlighting its potent and durable antitumor efficacy.

This platform offers several conceptual and practical advantages over conventional cancer therapies: (i) it introduces an engineered intracellular bacterium as an exogenous organelle to directly remodel tumor suppressor protein signaling; (ii) the QS-regulated lysis system enhances protein release while maintaining bacterial safety in vivo; (iii) the biohybrid design enables efficient intracellular delivery and sustained release of small-molecule therapeutics; and (iv) restoration of tumor suppressor function within tumor cells provides a fundamentally distinct and potentially safer therapeutic paradigm.

Nevertheless, several questions warrant further investigation. First, the immunological consequences of bacterial lysis-derived components, including DNA fragments that may activate the cGAS-STING pathway, remain to be elucidated. In addition, as the current studies were conducted in murine tumor models, future work using patient-derived xenograft models will be necessary to more accurately assess translational potential. In summary, the engineered VPE-PTEN@RG-NPs platform establishes a novel and versatile strategy for sustained restoration of tumor suppressor functions and represents a promising approach for effective cancer therapy.

MATERIALS AND METHODS

Materials

The cell lines used in this study, including 4T1, B16F10, RAW264.7, and DC2.4, were obtained from Meilun Biotechnology Co., Ltd. The luciferase-expressing 4T1 cell line (4T1-luc) was purchased from Wuhan Servicebio Biotechnology Co., Ltd. All cell lines were cultured in RPMI 1640 or DMEM supplemented with 10% FBS and 1% penicillin-streptomycin. Cells were maintained under standard culture conditions in a humidified incubator at 37°C with 5% CO_2. RG7388, N-hydroxysuccinimide (NHS),

and EDCI were purchased from Shanghai Bide Pharmaceutical Technology Co., Ltd. Poly(lactic-co-glycolic acid) (PLGA) was obtained from Shanghai Yuanye Bio-Technology Co., Ltd. Fluorescein isothiocyanate (FITC) was purchased from Energy Chemical, and DiR was purchased from Yeasen Biotechnology (Shanghai) Co., Ltd. RPMI 1640 medium and 0.25% trypsin-EDTA were obtained from Meilun Biotechnology Co., Ltd. Fetal bovine serum (FBS) and penicillin and streptomycin solution (PS) were purchased from Yeasen Biotechnology (Shanghai) Co., Ltd. MTT was purchased from Solarbio. LB broth and LB nutrient agar were all purchased from Haibo Biotechnology Co., Ltd. FITC was purchased from Energy Chemical. Collagenase I was purchased from Lanjieke Technology Co., Ltd.

Methods

Bacterial strains and plasmid construction. All bacterial strains were cultured in LB medium. Antibiotic-resistant bacterial strains were cultured in LB supplemented with kanamycin (50 μg/mL). To construct the VPE strain, a linear *pluxI-LysE* DNA fragment was integrated into the downstream of the *glmS* gene in the genome of VNP via Red/ET recombination. Successful genomic integration was confirmed by colony PCR using primers listed in **Table S1**, followed by agarose gel electrophoresis to verify the PCR products. For generation of the VNP-GFP and VNP-PTEN strains, the plasmids pBR322-*pluxI*-GFP and pBR322-*pluxI*-PTEN constructed by Tsingke Biotechnology Co., Ltd. were introduced into VNP-WT by electroporation at 1800 V with a time constant of 5 ms. The plasmid maps are presented in Fig. S18. The VPE-GFP and VPE-PTEN strains were generated using similar procedures. Additionally, VPE-WT transformed with the empty vector (pBR322-vector) was used as a control. Detailed information on all engineered bacterial strains and corresponding plasmids is summarized in **Table S2**, and the amino acid sequences of PTEN and LysE are provided in **Table S3**.

Characterization of the VPE strain. To evaluate QS-regulated lysis of the VPE strain, VNP-GFP and VPE-GFP were cultured on LB agar plates supplemented with kanamycin (50 μg/mL) at 37°C for 12 h, and colony morphology was examined by fluorescence microscopy. Meanwhile, the strain was grown in LB liquid medium containing kanamycin (50 μg/mL) at 37°C with shaking at 220 rpm. At predetermined time points (0, 3, 6, 7, 8.5, 9.5, and 12 h), bacterial cultures were collected and OD600 values were measured. Concurrently, bacterial suspensions and cell-free culture supernatants were collected for quantitative analysis of GFP fluorescence intensity. To further assess intracellular lysis of the VPE strain in tumor cells, VNP-GFP or VPE-GFP was co-incubated with 4T1 tumor cells at a multiplicity of infection (MOI) of 10 for 12 h. Subsequently, cells were thoroughly washed with PBS to remove extracellular bacteria, stained with DAPI to label nuclei, and imaged by fluorescence microscope to evaluate the intracellular distribution and release of GFP.

Western blot analysis. Bacterial pellets (intracellular fraction) and culture supernatants (extracellular fraction) were collected by centrifugation at 2000 × g at 4°C. Pellets were resuspended and lysed on ice for 10 min using Cell Lysis Buffer for Western blotting (Beyotime, P0013) supplemented with 1 mM phenylmethanesulfonyl fluoride (PMSF), followed by sonication on ice for 2 min. Culture supernatants were concentrated using 10 kDa molecular weight cutoff (MWCO) ultrafiltration units (Beyotime, FUF510) according to the manufacturer's instructions. Protein samples from tumor cells and tumor

tissues were prepared using the same protocol. Protein concentrations were determined using a BCA Protein Assay Kit (Yeasen, 20200ES76). Equal amounts of protein were separated by SDS–PAGE on 10% polyacrylamide gels and transferred onto PVDF membranes. Membranes were blocked with 5% non-fat milk in TBST for 1 h at room temperature and incubated overnight at 4°C with primary antibodies against PTEN (Servicebio, GB113803), p53 (Epizyme, R012089), phospho-AKT (Ser473) (Epizyme, R011470), cleaved caspase-3 (Epizyme, R013264), LC3B (Epizyme, R013940), and GAPDH (Proteintech, 60004-1-Ig). After washing with TBST, membranes were incubated with horseradish peroxidase (HRP)-conjugated secondary antibodies for 1 h at room temperature. Protein bands were visualized using an enhanced chemiluminescence (ECL) detection kit (Servicebio, G2161) following the manufacturer's instructions.

Evaluation of VPE-PTEN-induced M1 polarization of RAW264.7 cells in vitro. To assess the functional role of PTEN in macrophage polarization, single colonies of VPE-PTEN or VNP-WT were selected and cultured overnight in LB medium supplemented with kanamycin under shaking conditions. Culture supernatants were collected, concentrated, and applied to RAW264.7 macrophages seeded at a density of 1×10^6 cells per well in 6-well plates. After 24 h of incubation, the proportion of M1-polarized macrophages ($F4/80^+CD80^+$) was analyzed by flow cytometry.

Effect of VPE-PTEN on tumor cell proliferation. The impact of VPE-PTEN on tumor cell proliferation was assessed using an MTT assay. Briefly, 4T1 or B16F10 cells were seeded in a 96-well plate at a density of 1×10^4 cells per well. After 12 h, VPE-WT or VPE-PTEN was added at an MOI of 10 and co-cultured for 12 h. Afterward, cells were washed three times with PBS to remove non-invading bacteria, followed by incubation in DMEM supplemented with 1% PSA and 10% serum for an additional 24 h. Cell viability was determined by the addition of MTT solution (5 mg/mL).

The anti-migratory effect of VPE-PTEN. The anti-migratory activity of VPE-PTEN was assessed using a wound-healing assay. Briefly, 4T1 cells were seeded in a six-well plate at a density of 5×10^5 cells per well. After 12 h, VPE-WT or VPE-PTEN was added at an MOI of 10 and co-cultured for 12 h. Non-invading bacteria were removed by washing three times with PBS, and fresh serum-free medium was added. A linear scratch was then generated in each well using a sterile 20 μL pipette tip, and images were captured immediately (0 h). The same scratch areas were imaged at 10, 20, and 30 h. All experiments were performed independently in triplicate.

Evaluation of VPE-PTEN-mediated apoptosis and autophagy in tumor cells. To evaluate VPE-PTEN-induced apoptosis, 4T1 or B16F10 cells were seeded in 6-well plates at a density of 5×10^5 cells per well and co-incubated with VPE-WT or VPE-PTEN at an MOI of 10 for 24 h. Cells were then harvested and stained using an Annexin V-FITC/PI Apoptosis Kit (MULTI SCIENCES, AT101), followed by flow cytometry analysis. To evaluate autophagy, 4T1 cells were seeded at 5×10^5 cells per well and treated with VPE-WT or VPE-PTEN for 24 h. Cells were then collected for protein extraction, and LC3B expression was analyzed by western blotting. In addition, LC3B localization was visualized by immunofluorescence staining. Briefly, treated cells were washed with PBS, fixed, permeabilized, and incubated with an anti-LC3B primary antibody at 4°C overnight. After washing, cells were incubated with a CoraLite® Plus 594

Goat Anti-Rabbit Secondary Antibody (Proteintech, RGAR004) for 1 h at room temperature. Nuclei were counterstained with DAPI, and fluorescence images were acquired using a confocal laser scanning microscope. To further determine the effect of VPE-PTEN-induced autophagy on DC cell maturation, conditioned media from 4T1 cells treated with VPE-WT or VPE-PTEN for 48 h were transferred to DC2.4 cells and incubated for 24 h. The proportion of mature DCs ($CD40^+$ MHC I^+) was subsequently quantified by flow cytometry.

Preparation and characterization of RG-NPs. RG7388-loaded nanoparticles (RG-NPs) were prepared using a double-emulsion solvent evaporation method. Briefly, PLGA (25 mg) and RG7388 (1 mg) were dissolved in 3 mL of dichloromethane, followed by the addition of 3 mL of 1% (w/v) polyvinyl alcohol (PVA) and ultrasonic emulsification. The resulting emulsion was then added dropwise to 15 mL of 0.05% PVA solution under continuous stirring. After stirring at room temperature for 2 h, RG-NPs were collected by centrifugation. The particle size and zeta potential were measured by dynamic light scattering (DLS), and morphology was examined using transmission electron microscopy (TEM). To evaluate the pH-responsive drug release, RG-NPs were placed in a dialysis bag (molecular weight cutoff, 2 kDa) and immersed in release media at pH 7.4 or 6.5 (deionized water containing 0.5% Tween 80) under gentle agitation. At predetermined time points, 100 μL of the dialysate was collected, and nanoparticles were lysed with methanol. The RG7388 content was then quantified by high-performance liquid chromatography (HPLC) using a mobile phase of methanol/water (85/15, v/v) at a flow rate of 1 mL/min, with UV detection at 195 nm.

Preparation and characterization of VPE-PTEN@RG-NPs. VPE-PTEN@RG-NPs was prepared via carbodiimide-mediated coupling. Briefly, EDCI and NHS were added to RG-NPs solutions and gently stirred at room temperature for 1 h to activate surface carboxyl groups. Pre-cultured VPE-PTEN bacteria were then added, and the mixture was gently stirred at room temperature for an additional 30 min to enable covalent conjugation of the nanoparticles to the bacterial surface. The resulting VPE-PTEN@RG-NPs were collected via centrifugation at 4500 rpm for 5 min. The morphology and surface distribution of RG-NPs on bacteria were examined by TEM. In addition, VPE-PTEN@FITC-NPs were prepared using the same procedure, and FITC fluorescence on the bacterial surface was visualized by fluorescence microscopy. To evaluate the effect of RG-NPs on bacterial growth, VNP@RG-NPs were prepared with unmodified VNP serving as the control. The OD600 absorbance was measured at 30 min intervals using a microplate reader, and growth curves were plotted accordingly.

Evaluation of the targeted delivery of VPE-PTEN-NPs. Targeted delivery of VPE-PTEN-conjugated nanoparticles was first evaluated using a three-dimensional (3D) in vitro spheroid model. Briefly, 60 μL of DMEM containing 1.5% agarose was added to each well of a 96-well plate. After gel solidification, 2×10^3 4T1 cells were seeded per well and incubated in a cell culture incubator. Tumor spheroids were monitored microscopically and used for subsequent experiments once their diameters reached approximately 300 μm. VPE-PTEN@FITC-NPs or FITC-NPs were then added to the spheroids. After 24 h of incubation, spheroids were washed with PBS and imaged by confocal microscopy with Z-stack acquisition to visualize the intratumoral distribution of FITC fluorescence. The in vivo targeting efficacy

of VPE-PTEN-mediated nanoparticle delivery was further evaluated using a 4T1 subcutaneous tumor-bearing mouse model. Briefly, 1.5×10^6 4T1 cells were subcutaneously inoculated into BALB/c mice. When tumor volumes reached approximately 250 mm^3, mice were randomly assigned to two groups (n = 5) and intravenously injected with either VPE-PTEN@DiR-NPs or DiR-NPs alone (5 mg/kg DiR-NPs). DiR fluorescence signals at tumor sites were monitored using an IVIS imaging system.

In vivo distribution of VPE-PTEN. To investigate the biodistribution of VPE-PTEN and evaluate the expression levels of PTEN in tumor tissues, an orthotopic 4T1 breast cancer model was established in BALB/c mice. Briefly, 1.5×10^6 4T1 cells were orthotopically implanted into the mammary fat pad. When tumor volumes reached 80–100 mm^3, mice were randomly assigned to two groups (n = 5). VNP-PTEN or VPE-PTEN (1×10^6 CFU) was administered intravenously via the tail vein on days 0, 3, and 6. On day 8, major organs (heart, liver, spleen, lung, and kidney) and tumor tissues were harvested, homogenized, and plated onto LB agar plates supplemented with kanamycin. After overnight incubation, bacterial colonies were counted to determine bacterial distribution. PTEN expression levels in tumor tissues were also analyzed by western blotting.

In vivo anti-tumor efficacy studies. All animal experiments were approved by the Institutional Animal Care and Use Committee of Ocean University of China and conducted in accordance with the institutional guidelines. To establish subcutaneous and lung metastasis melanoma models, B16F10 cells (1×10^6) were inoculated subcutaneously into C57 mice on day − 7, and an additional 5×10^5 cells were injected intravenously via the tail vein on day − 1. When subcutaneous tumors reached 80–100 mm^3, mice were randomly assigned to six groups and treated with PBS, VPE-WT (1×10^6 CFU), VPE-PTEN (1×10^6 CFU), RG-NPs (5 mg/kg), VPE-PTEN + RG-NPs (1×10^6 CFU + 5 mg/kg), or VPE-PTEN@RG-NPs (1×10^6 CFU + 5 mg/kg) intravenously on days 0, 3, and 6. Tumor volumes (length × $width^2/2$) and body weights were recorded every two days. On day 10, tumors were harvested, photographed, and weighed. Tumor inhibition rates were analyzed. Meanwhile, tumor volume doubling time was calculated using the formula $TVDT = (\Delta t \times \ln(2)) / \ln(V2/V1)$, where Δt represents the time interval between measurements, and V1 and V2 denote tumor volumes at the initial and final measurements, respectively. Moreover, tumor sections were subjected to immunofluorescence staining to detect PTEN and p53 expression, while necrosis and apoptosis were assessed by H&E and TUNEL staining.

To further evaluate the therapeutic efficacy, an orthotopic 4T1 breast cancer model was established by implanting 1.5×10^6 4T1 cells into the mammary fat pad of 8-week-old female BALB/c mice. Once tumors reached 80–100 mm^3, mice were randomly divided into six groups (n = 5) and treated intravenously with PBS, VPE-WT (1×10^6 CFU), VPE-PTEN (1×10^6 CFU), RG-NPs (5 mg/kg), VPE-PTEN + RG-NPs (1×10^6 CFU + 5 mg/kg), or VPE-PTEN@RG-NPs (1×10^6 CFU + 5 mg/kg) on days 0, 3, and 6. Tumor volumes and body weights were recorded every two days. On day 21, tumors were harvested for weighing and histological analysis. H&E and TUNEL staining were performed to assess tumor morphology and apoptosis. For biosafety evaluation, major organs and blood samples were collected from the PBS and VPE-PTEN@RG-NPs groups for histopathological examination and complete blood count analysis. To evaluate systemic antitumor immune responses, a bilateral 4T1 tumor model was established. Primary tumors were

induced by subcutaneous injection of 4T1 cells into the right flank of BALB/c mice on day − 7, followed by implantation of secondary tumors into the left flank five days later. When the primary tumor volume reached 80–100 mm^3, PBS or VPE-PTEN@RG-NPs (1×10^6 CFU + 5 mg/kg) were administered intratumorally. Tumor volumes on both sides were monitored every two days using the formula "length × $width^2$ × 0.5." On day 21, tumors were excised, photographed, and weighed.

To further evaluate the efficacy of the combination of VPE-PTEN@RG-NPs and aPD-1, a 4T1-luc breast cancer mouse model was established by inoculating 2×10^6 4T1-luc cells into the dorsal region of BALB/c mice. When tumors reached 80–100 mm^3, mice were randomly assigned to four groups (n = 5) and treated with PBS, aPD-1 (2.5 mg/kg), VPE-PTEN@RG-NPs (1×10^6 CFU + 5 mg/kg), or a combination of VPE-PTEN@RG-NPs (1×10^6 CFU + 5 mg/kg) and aPD-1 (2.5 mg/kg). The aPD-1 was administered on days 0, 3, and 6, while VPE-PTEN@RG-NPs were injected on days 1, 4, and 7. At designated time points, D-luciferin potassium salt (3 mg per mouse) was administered intraperitoneally, and bioluminescence imaging was performed using an IVIS system. Mouse survival was monitored for up to 80 days, with death defined as tumor volume > 2000 mm^3.

Evaluation of the in vivo immunostimulatory effects of VPE-PTEN@RG-NPs. To assess immune activation induced by treatment, subcutaneous tumor tissues from the B16F10 melanoma model were harvested on day 10 and analyzed by flow cytometry. Briefly, tumors were enzymatically digested with type I collagenase at 37°C for 1 h and filtered through a 40-μm cell strainer to obtain single-cell suspensions. Cells were stained with specific antibodies to identify immune populations: macrophages (CD11b, F4/80, CD80, and CD206), $CD8^+$ T cells (CD3, CD8), Treg cells (CD4, FOXP3), and dendritic cells (CD40, MHCII). Labeled cells were then analyzed by flow cytometry. In addition, immunofluorescence staining was performed on tumor sections to visualize the infiltration of $CD8^+$ T cells and M1-type macrophages.

Enzyme-linked Immunosorbent Assay (ELISA). Tumor tissues were harvested from mice, weighed, and minced into 1–2 mm^3 fragments. Subsequently, the tissue fragments were incubated in DMEM supplemented with type I collagenase (1 mg/mL) and $CaCl_2$ (0.3 mg/mL) and digested for 1 h at 37°C under gentle agitation on an orbital shaker. Following digestion, samples were centrifuged at 12,000 × g for 5 min at 4°C to pellet cellular debris. The clarified supernatant was collected and stored at -80°C until further analysis. TNF-α and IL-1β concentrations in the supernatants were quantified using commercially available ELISA kits (Thermo Fisher Scientific Inc.), according to the manufacturer's instructions.

Statistical analysis. Statistical analysis was performed using GraphPad Prism software. Student's *t*-test was applied for comparisons between two groups, while one-way ANOVA followed by Tukey's or Fisher's LSD test was used for multiple group comparisons. A value of $P < 0.05$ was considered statistically significant, and the following significance levels were assigned: (ns) $P > 0.05$, *$P < 0.05$, **$P < 0.01$, ***$P < 0.001$.

Declarations

Acknowledgments

This work was supported by grants from the National Natural Science Foundations of China (Nos. 32370096 and 82003622), the Natural Science Foundation of Shandong Province for Distinguished Young Scholars (Overseas, 2023HWYQ-068), the Taishan Scholar Foundation of Shandong Province for Young Experts (tsqn202312092), and the start-up package from the Ocean University of China.

Data Availability

The authors declare that all the data supporting the findings of this study are available within the article and Supplementary Information.

Ethics approval and consent to participate

All animal experimental procedures were conducted according to all relevant ethical regulations and strictly followed the protocols approved by the Institutional Animal Care and Use Committee at the Ocean University of China.

Supporting information

Supporting information is available from the electronic link or from the author.

Competing Interest

The authors declare no competing interests.

References

1. Blair LM et al (2023) Oncogenic context shapes the fitness landscape of tumor suppression. Nat Commun 14:6422
2. Krupina K, Goginashvili A, Cleveland DW (2024) Scrambling the genome in cancer: causes and consequences of complex chromosome rearrangements. Nat Rev Genet 25:196–210
3. Qian H et al (2023) Super-enhancers and the super-enhancer reader BRD4: tumorigenic factors and therapeutic targets. Cell Death Discov 9:470
4. Yu X et al (2024) Cancer epigenetics: from laboratory studies and clinical trials to precision medicine. Cell Death Discov 10:28
5. Shi W et al (2023) Immune checkpoint B7-H3 is a therapeutic vulnerability in prostate cancer harboring PTEN and TP53 deficiencies. Sci Transl Med 15:eadf6724
6. Shen WH et al (2007) Essential role for nuclear PTEN in maintaining chromosomal integrity. Cell 128:157–170
7. Serebriiskii IG et al (2022) Comprehensive characterization of PTEN mutational profile in a series of 34,129 colorectal cancers. Nat Commun 13:1618

8. Li Y, Ma R, Hao X (2024) Therapeutic role of PTEN in tissue regeneration for management of neurological disorders: stem cell behaviors to an in-depth review. Cell Death Dis 15:268
9. Qi Z et al (2022) Overcoming resistance to immune checkpoint therapy in PTEN-null prostate cancer by intermittent anti-PI3Kα/β/δ treatment. Nat Commun 13:182
10. Zhang C et al (2024) Secreted PTEN binds PLXDC2 on macrophages to drive antitumor immunity and tumor suppression. Dev Cell 59:3072–3088e3078
11. Bergholz JS et al (2023) PI3Kβ controls immune evasion in PTEN-deficient breast tumours. Nature 617:139–146
12. Wang H, Guo M, Wei H, Chen Y (2023) Targeting p53 pathways: mechanisms, structures, and advances in therapy. Signal Transduct Target Ther 8:92
13. Kaiser AM et al (2023) p53 governs an AT1 differentiation programme in lung cancer suppression. Nature 619:851–859
14. Chen M et al (2022) A p53-phosphoinositide signalosome regulates nuclear AKT activation. Nat Cell Biol 24:1099–1113
15. Freeman DJ et al (2003) PTEN tumor suppressor regulates p53 protein levels and activity through phosphatase-dependent and -independent mechanisms. Cancer Cell 3:117–130
16. Singh S et al (2025) Glioblastoma at the crossroads: current understanding and future therapeutic horizons. Signal Transduct Target Ther 10:213
17. Treekitkarnmongkol W et al (2024) eEF1A2 promotes PTEN-GSK3β-SCF complex-dependent degradation of Aurora kinase A and is inactivated in breast cancer. Sci Signal 17:eadh4475
18. Kim Y et al (2024) Design of PD-L1-Targeted Lipid Nanoparticles to Turn on PTEN for Efficient Cancer Therapy. Adv Sci (Weinh) 11:e2309917
19. Navaridas R et al (2023) In Vivo Intra-Uterine Delivery of TAT-Fused Cre Recombinase and CRISPR/Cas9 Editing System in Mice Unveil Histopathology of Pten/p53-Deficient Endometrial Cancers. Adv Sci (Weinh) 10:e2303134
20. Gurbatri CR, Arpaia N, Danino T (2022) Engineering bacteria as interactive cancer therapies. Science 378:858–864
21. Cooper RM et al (2023) Engineered bacteria detect tumor DNA. Science 381:682–686
22. Zhang Y, Buchholz F, Muyrers JP, Stewart AF (1998) A new logic for DNA engineering using recombination in Escherichia coli. Nat Genet 20:123–128
23. Liu Z et al (2026) Chemo-immunotherapeutic potential of Lactobacillus rhamnosus GG and its bioengineering for cancer therapy. Biomaterials 328:123848
24. Kwon SY, Thi-Thu Ngo H, Son J, Hong Y, Min JJ (2024) Exploiting bacteria for cancer immunotherapy. Nat Rev Clin Oncol 21:569–589
25. Guan Q et al (2025) Biocompatible cloaking of bacteria for effective tumor imaging and therapy. Mater Today Bio 32:101788

26. Harimoto T et al (2022) A programmable encapsulation system improves delivery of therapeutic bacteria in mice. Nat Biotechnol 40:1259–1269
27. Hurt RC et al (2023) Genomically mined acoustic reporter genes for real-time in vivo monitoring of tumors and tumor-homing bacteria. Nat Biotechnol 41:919–931
28. Savage TM et al (2023) Chemokines expressed by engineered bacteria recruit and orchestrate antitumor immunity. Sci Adv 9:eadc9436
29. Li R, Li A, Zhang Y, Fu J (2023) The emerging role of recombineering in microbiology. Eng Microbiol 3:100097
30. Chen M, Liu J (2025) Regulating Bacteria-Host Interactions for Disease Intervention by Covalent Conjugation of Bacterial Surface. Acc Chem Res 58:2110–2123
31. Zhang Y, Muyrers JP, Rientjes J, Stewart AF (2003) Phage annealing proteins promote oligonucleotide-directed mutagenesis in Escherichia coli and mouse ES cells. BMC Mol Biol 4:1
32. Lin Z et al (2024) In situ immunomodulation of tumors with biosynthetic bacteria promote anti-tumor immunity. Bioact Mater 32:12–27
33. Toso JF et al (2002) Phase I study of the intravenous administration of attenuated Salmonella typhimurium to patients with metastatic melanoma. J Clin Oncol 20:142–152
34. Raman V et al (2021) Intracellular delivery of protein drugs with an autonomously lysing bacterial system reduces tumor growth and metastases. Nat Commun 12:6116
35. Li Z et al (2022) Enhancing Gasdermin-induced tumor pyroptosis through preventing ESCRT-dependent cell membrane repair augments antitumor immune response. Nat Commun 13:6321
36. Liu L et al (2023) A bacteria-based system expressing anti-TNF-α nanobody for enhanced cancer immunotherapy. Signal Transduct Target Ther 8:134
37. Ahmed SG et al (2022) Intratumoral injection of schwannoma with attenuated Salmonella typhimurium induces antitumor immunity and controls tumor growth. Proc Natl Acad Sci U S A 119:e2202719119
38. Din MO et al (2016) Synchronized cycles of bacterial lysis for in vivo delivery. Nature 536:81–85
39. Hassan AS et al (2023) Salmonella Typhimurium expressing chromosomally integrated Schistosoma mansoni Cathepsin B protects against schistosomiasis in mice. NPJ Vaccines 8:27
40. Whiteley M, Diggle SP, Greenberg EP (2017) Progress in and promise of bacterial quorum sensing research. Nature 551:313–320
41. Kong LR et al (2024) A glycolytic metabolite bypasses two-hit tumor suppression by BRCA2. *Cell* 187, 2269–2287.e2216
42. Yang Z, Sun JK, Lee MM, Chan MK (2022) Restoration of p53 activity via intracellular protein delivery sensitizes triple negative breast cancer to anti-PD-1 immunotherapy. J Immunother Cancer 10
43. Islam MA et al (2018) Author Correction: Restoration of tumour-growth suppression in vivo via systemic nanoparticle-mediated delivery of PTEN mRNA. Nat Biomed Eng 2:968

44. Tang G et al (2025) Repurposing MDM2 inhibitor RG7388 for TP53-mutant NSCLC: a p53-independent pyroptotic mechanism via ROS/p-p38/NOXA/caspase-3/GSDME axis. Cell Death Dis 16:452
45. Kreitz J et al (2023) Programmable protein delivery with a bacterial contractile injection system. Nature 616:357–364
46. Kim H et al (2025) Lipid nanoparticle-mediated mRNA delivery to CD34(+) cells in rhesus monkeys. Nat Biotechnol 43:1813–1820

Schemes

Scheme 1 is available in the Supplementary Files section

Figures

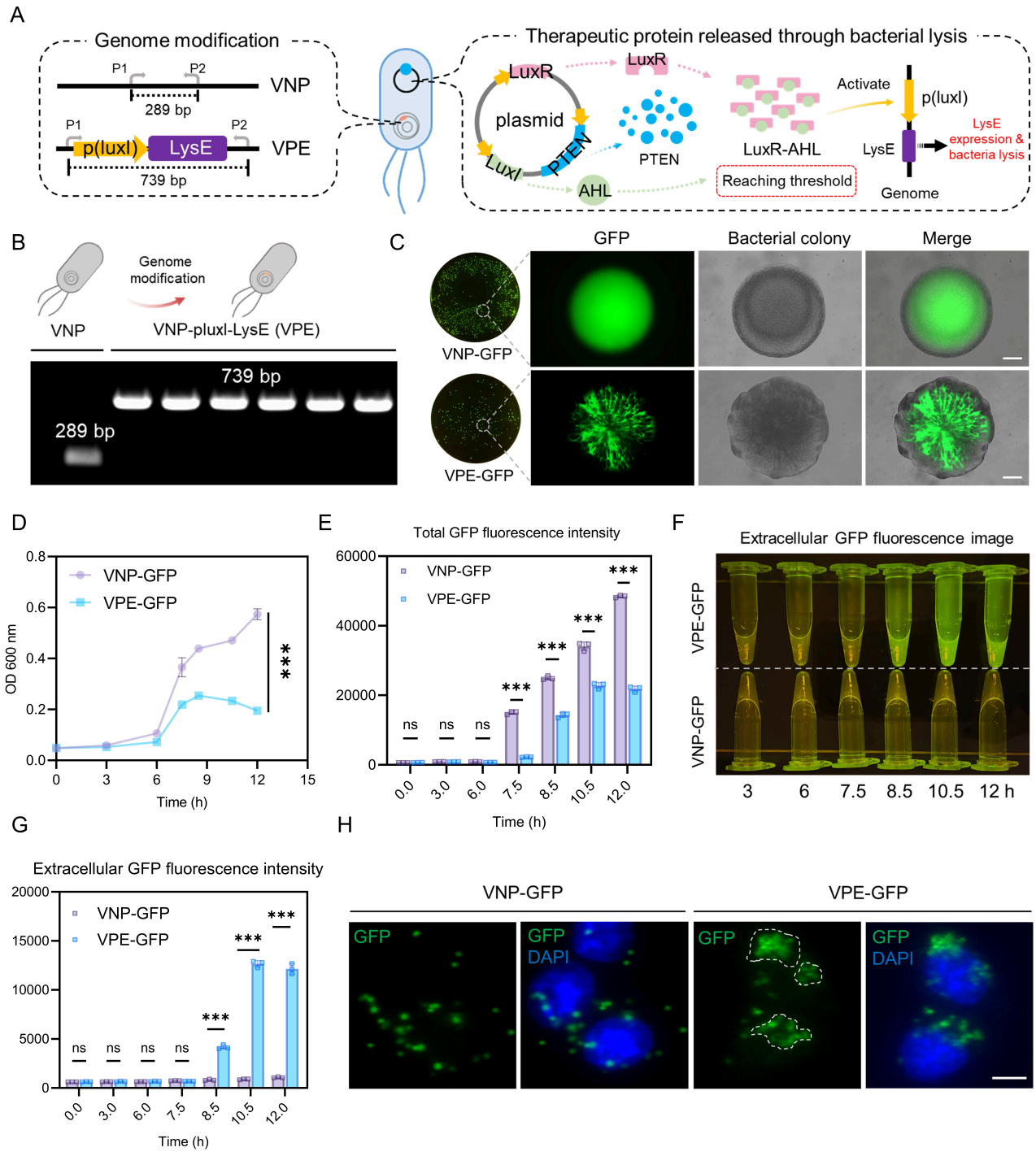


Figure 1

Construction and characterization of the VPE. (**A**) Schematic illustration of the QS-regulated lysis system in VPE-PTEN and the corresponding controlled release of PTEN. (**B**) Agarose gel electrophoresis analysis confirming genomic integration of the *pluxI-LysE* fragment. (**C**) Representative fluorescence images of GFP-expressing bacterial colonies (VNP-GFP and VPE-GFP). Scale bar, 80 μm. (**D**) Growth curves of VNP and VPE monitored via a microplate reader. (**E**) Time-dependent fluorescence intensities

of VNP-GFP and VPE-GFP cultures. (**F**) Representative fluorescence images and (**G**) quantitative analysis of GFP fluorescence in the extracellular culture medium of VNP-GFP and VPE-GFP at different time points under blue light (470 nm) irradiation. (**H**) Fluorescence images of 4T1 cells after co-incubation with VNP-GFP or VPE-GFP. The green color represents the GFP-expressed VNP or VPE, and the blue color represents DAPI-labeled nuclei. Scale bar, 20 μm. Data were presented as mean ± s.d. (n = 3). Statistical analysis was performed using two-way ANOVA (**D**, **E**, and **G**). ****P* < 0.001, n.s., no significance.

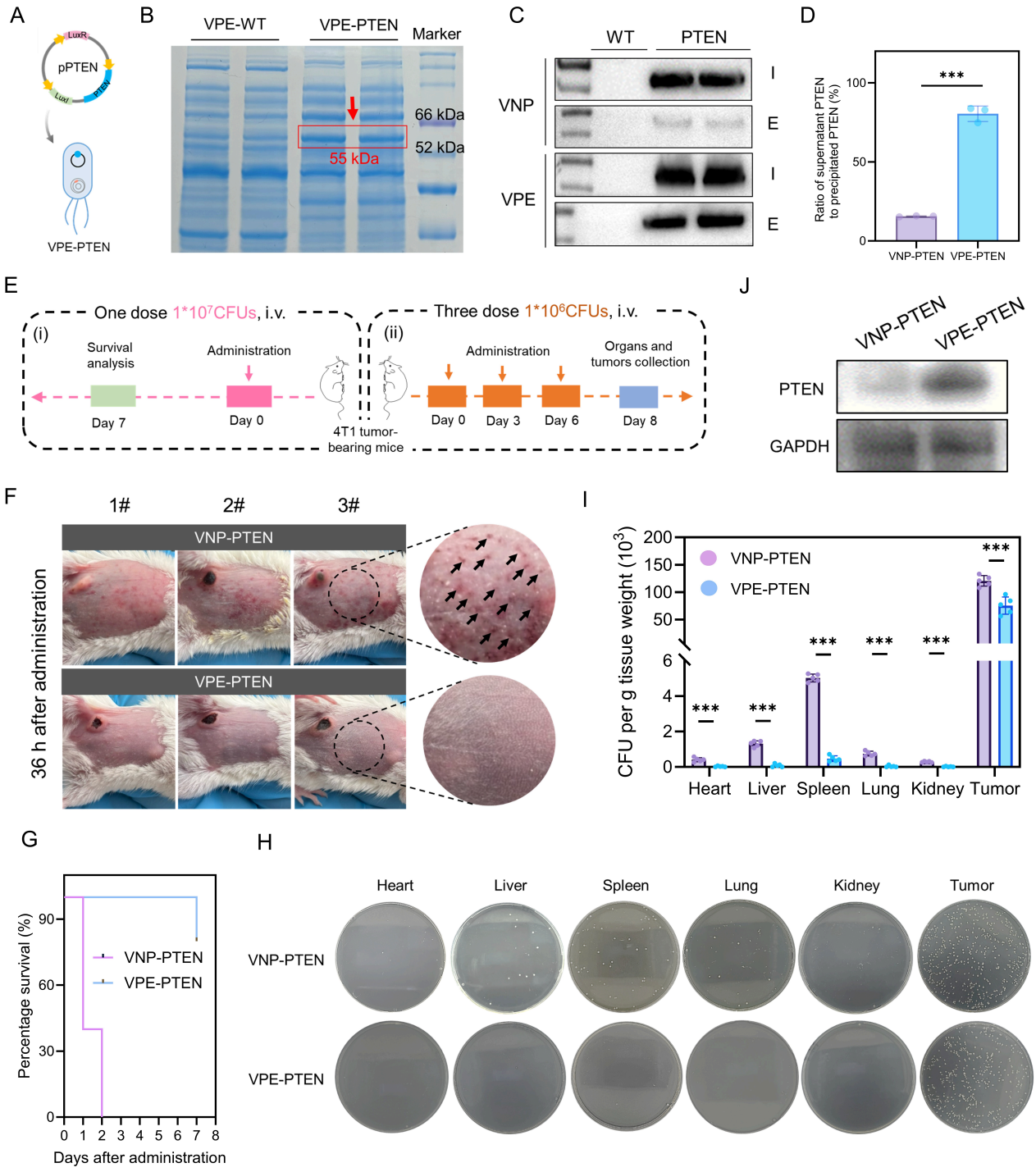


Figure 2

Verification of PTEN expression and safety evaluation of VPE-PTEN. (**A**) Schematic illustration of the construction of VPE-PTEN. (**B**) SDS-PAGE analysis confirming PTEN expression by VPE-PTEN, with VPE-WT used as a control. (**C**) Western blot analysis of PTEN levels in intracellular (I) and extracellular (E) fractions of VNP and VPE cultures. (**D**) Quantification of the extracellular-to-intracellular PTEN ratio. Data are presented as means ± s.d. (n = 3). (**E**) Schematic of the in vivo experimental protocols: intravenous injection of 1×10^7 CFU per mouse to evaluate the safety profile of VPE-PTEN (i) or 1×10^6 CFU three times per mouse to assess the biodistribution (ii). (**F**) Representative images of mouse morphology after treatment with VNP-PTEN or VPE-PTEN for 36 h. (**G**) Survival curves of mice treated with VNP-PTEN or VPE-PTEN (n = 5). (**H**) Biodistribution of VPE-PTEN in tumors and major organs, determined by plate spreading. (**I**) The quantified numbers of bacteria in tumors and major organs after VNP-PTEN or VPE-PTEN treatment (n = 5). (**J**) PTEN levels in tumor tissues after VPE-PTEN or VNP-PTEN treatment, analyzed by western blot. (n = 5). Statistical analysis was performed using Student's *t*-test (**D**) and two-way ANOVA (**I**). ***$P < 0.001$.

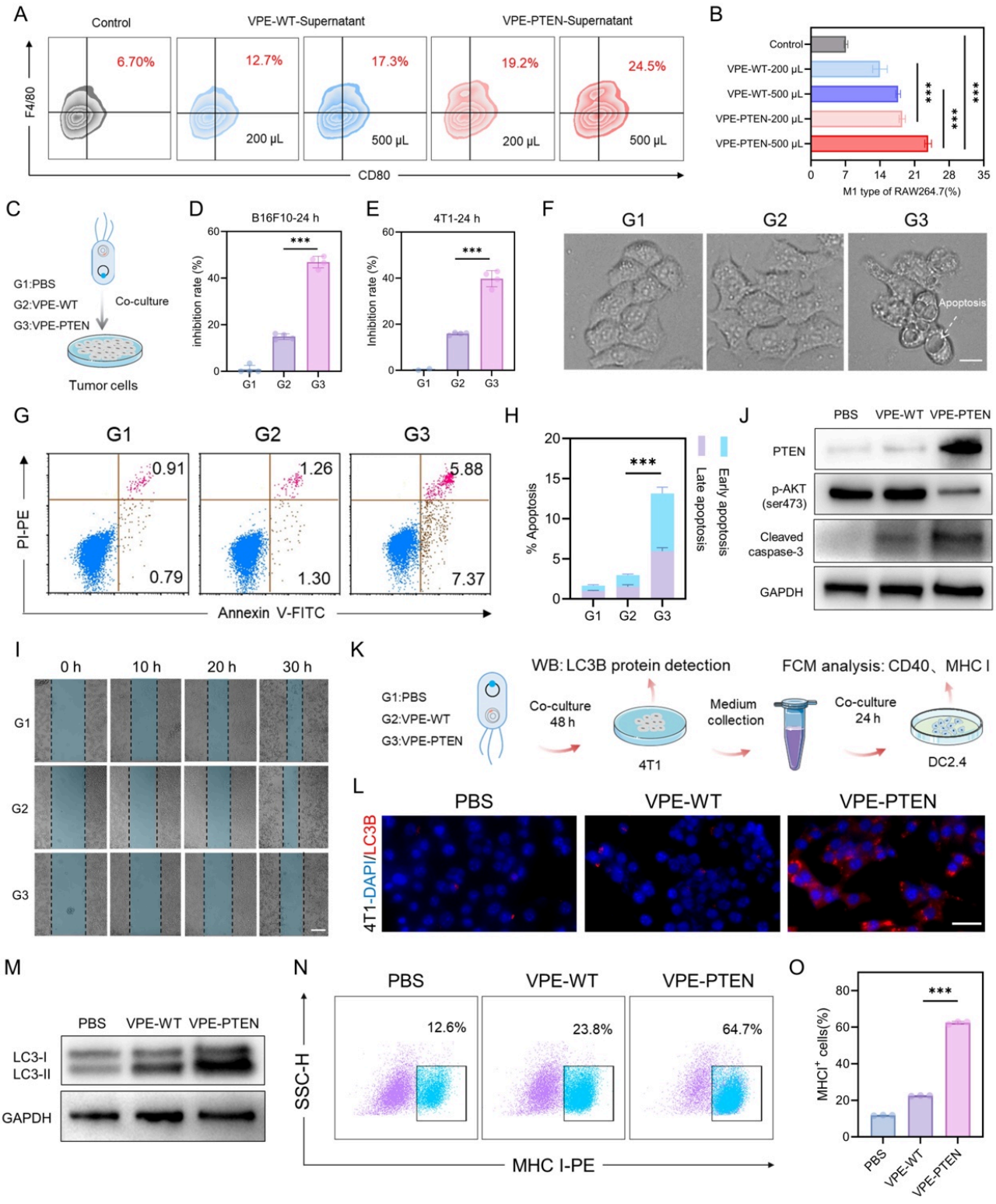


Figure 3

In vitro evaluation of the anti-tumor activity of VPE-PTEN. (**A**) Representative flow cytometry plots of $F4/80^{+}CD80^{+}$ macrophages following treatment of RAW264.7 cells with concentrated supernatants from VPE-WT or VPE-PTEN cultures. (**B**) Quantitative analysis of M1-type macrophages. (**C**) Schematic illustration of the experimental design used to evaluate the antitumor effects of VPE-PTEN on tumor cells. (**D** and **E**) The inhibitory effect of VPE-PTEN or VPE-WT on B16F10 and 4T1 cells after 24 h

treatment, determined by MTT assay. (**F**) Representative morphological changes of tumor cells after incubation with VPE-PTEN or VPE-WT. Scale bar, 15 μm. (**G**) Representative flow cytometry plots of apoptotic tumor cells following VPE-PTEN or VPE-WT treatment, assessed by Annexin/PI staining. (**H**) Quantification of apoptotic cells. (**I**) Inhibition of tumor cell migration by VPE-PTEN, assessed by scratch wound assay. Scale bar, 200 μm. (**J**) Western blot analysis of apoptosis-related proteins in 4T1 cells after treatment with VPE-PTEN or VPE-WT. (**K**). Schematic illustration of VPE-PTEN-induced tumor cell autophagy and subsequent DC cell maturation. (**L**) Immunofluorescence images of LC3B in 4T1 cells treated with VPE-PTEN or VPE-WT for 36 h. Scale bar, 60 μm. (**M**) Western blot analysis of LC3B expression in 4T1 cells. (**N**) Representative flow cytometry plots of MHC I expressions on DCs. (**O**) Quantification of MHC I^+ DCs in VPE-PTEN or VPE-WT treatment groups. Data are presented as mean ± s.d. (n = 3). Statistical analysis was performed by one-way ANOVA. ***$P < 0.001$.

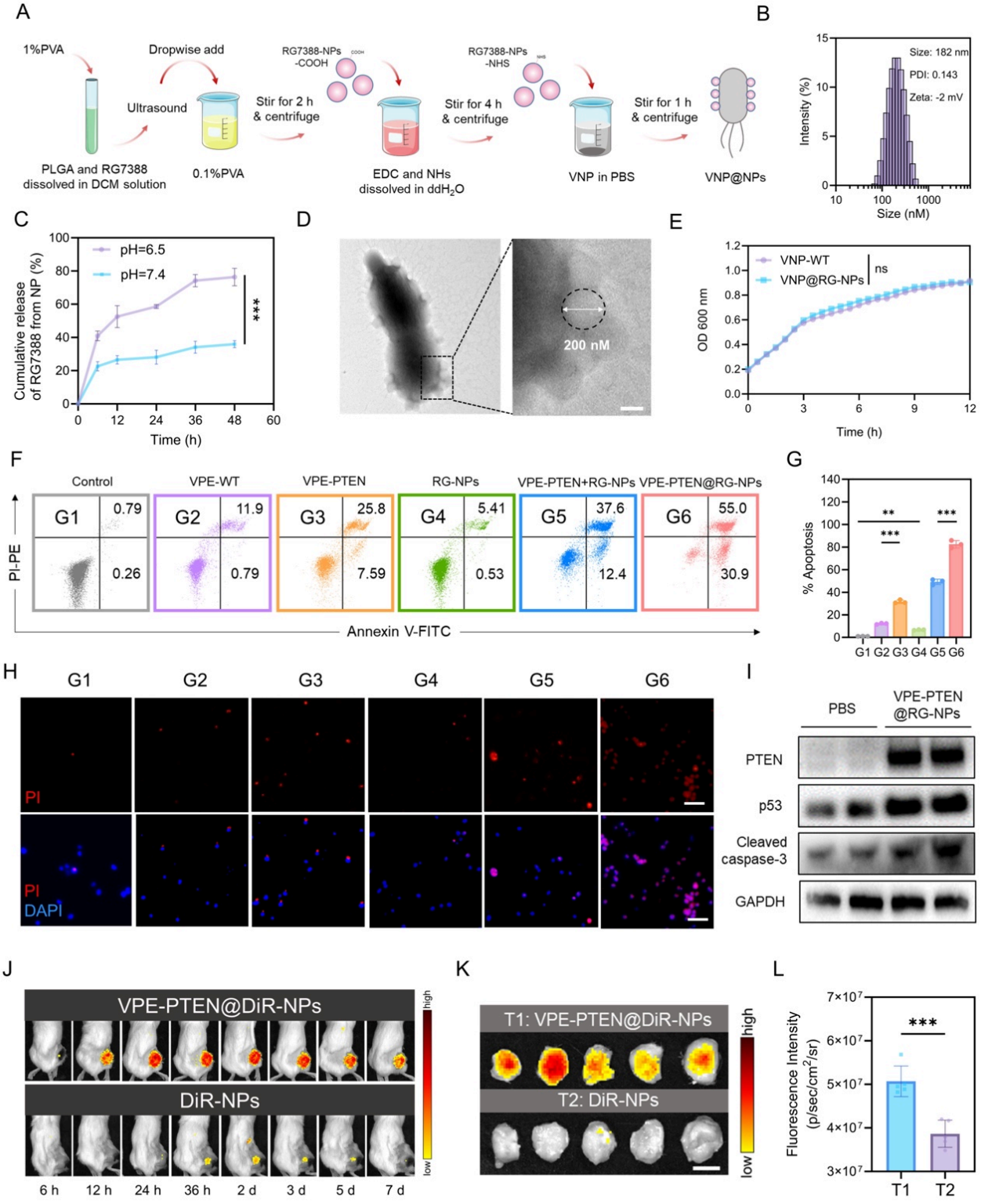


Figure 4

Construction of VPE-PTEN@RG-NPs and its antitumor potential evaluation. (**A**) Schematic illustration of the preparation of VPE-PTEN@RG-NPs. (**B**) The average size of RG-NPs measured by DLS. (**C**) In vitro release profiles of RG7388 from RG-NPs under pH 7.4 and pH 6.5 conditions. (**D**) Representative TEM image of RG-NPs conjugated to VPE (VPE-PTEN@RG-NPs). Scale bar, 100 nm. (**E**) Growth curves of VPE cultured in LB medium with or without RG-NPs conjugation, monitored via a microplate reader. (**F** and **G**)

Representative flow cytometry plots and quantitative analysis of apoptotic tumor cells following different treatments. (**H**) Representative fluorescence images of tumor cells after incubation with different treatments. The red color represents PI-labeled dead cells. Scale bar, 150 μm. (**I**) Western blot analysis of PTEN, p53, and cleaved caspase-3 expression in tumor cells treated with VPE-PTEN@RG-NPs. (**J**) IVIS images of 4T1 tumor-bearing mice following intravenous administration of VPE-PTEN@DiR-NPs or DiR-NPs. (**K**) The fluorescence images of isolated tumors 7 days after treatment. (n = 5). Scale bar, 5 mm. (**L**) Quantification of DiR fluorescence intensity in tumor tissues. Data are presented as mean ± s.d. (n = 3 or 5). Statistical analysis was performed using Student's *t*-test (**L**), one-way ANOVA (**G**), or two-way ANOVA (**C** and **E**). $^{**}P < 0.01$, $^{***}P < 0.001$, n.s., no significance.

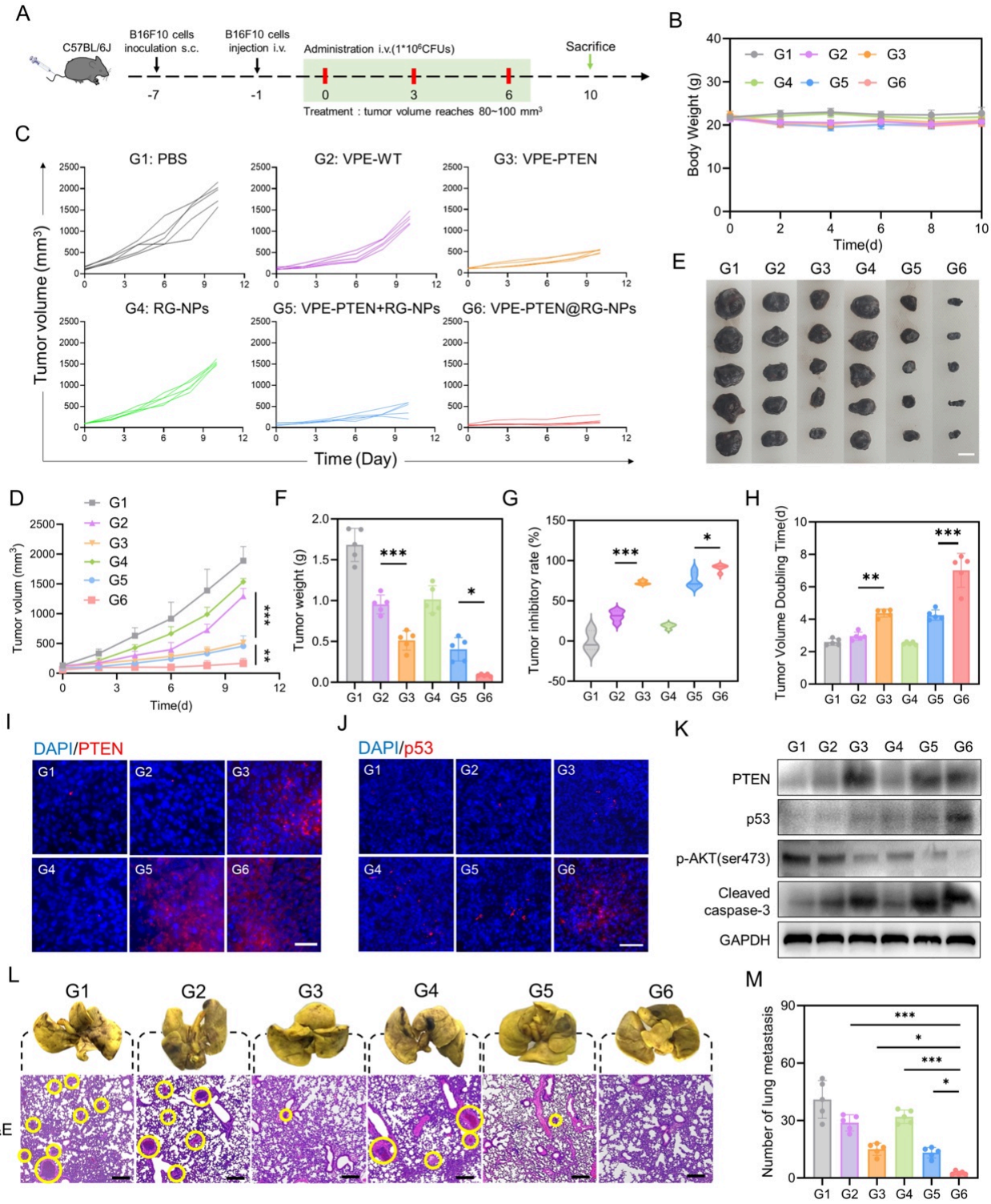


Figure 5

Evaluation of the antitumor efficacy of VPE-PTEN@RG-NPs in melanoma models. (**A**) Schematic illustration of the establishment and treatment protocols for subcutaneous and lung metastasis melanoma mouse models. (**B**) Changes in mouse body weight during the treatment period. (**C** and **D**) Tumor growth curves for the different treatment groups. (**E**) Representative images of excised tumor tissues. Scale bar, 3.5 mm. (**F**) Quantified tumor weight among different treatment groups. (**G**) Tumor

inhibition rates in different treatment groups. (**H**) Tumor volume doubling time. (**I** and **J**) Representative confocal immunofluorescence images showing PTEN (**I**) and p53 (**J**) expression in tumor tissues. Scale bar, 150 μm. (**K**) Western blot analysis of apoptosis-related proteins, including PTEN, p53, p-AKT (Ser473), and cleaved caspase-3, in tumor tissues. (**L**) Representative images of lungs after fixation in Bouin's solution and H&E staining in different treatment groups. Scale bar, 300 μm. (**M**) Quantification of metastatic nodules on the lung surface. Data are presented as mean ± s.d. (n = 5). Statistical analysis was performed using one-way ANOVA (**F**, **G, H,** and **M**) or two-way ANOVA (**D**). *P < 0.05, **P < 0.01, ***P < 0.001.

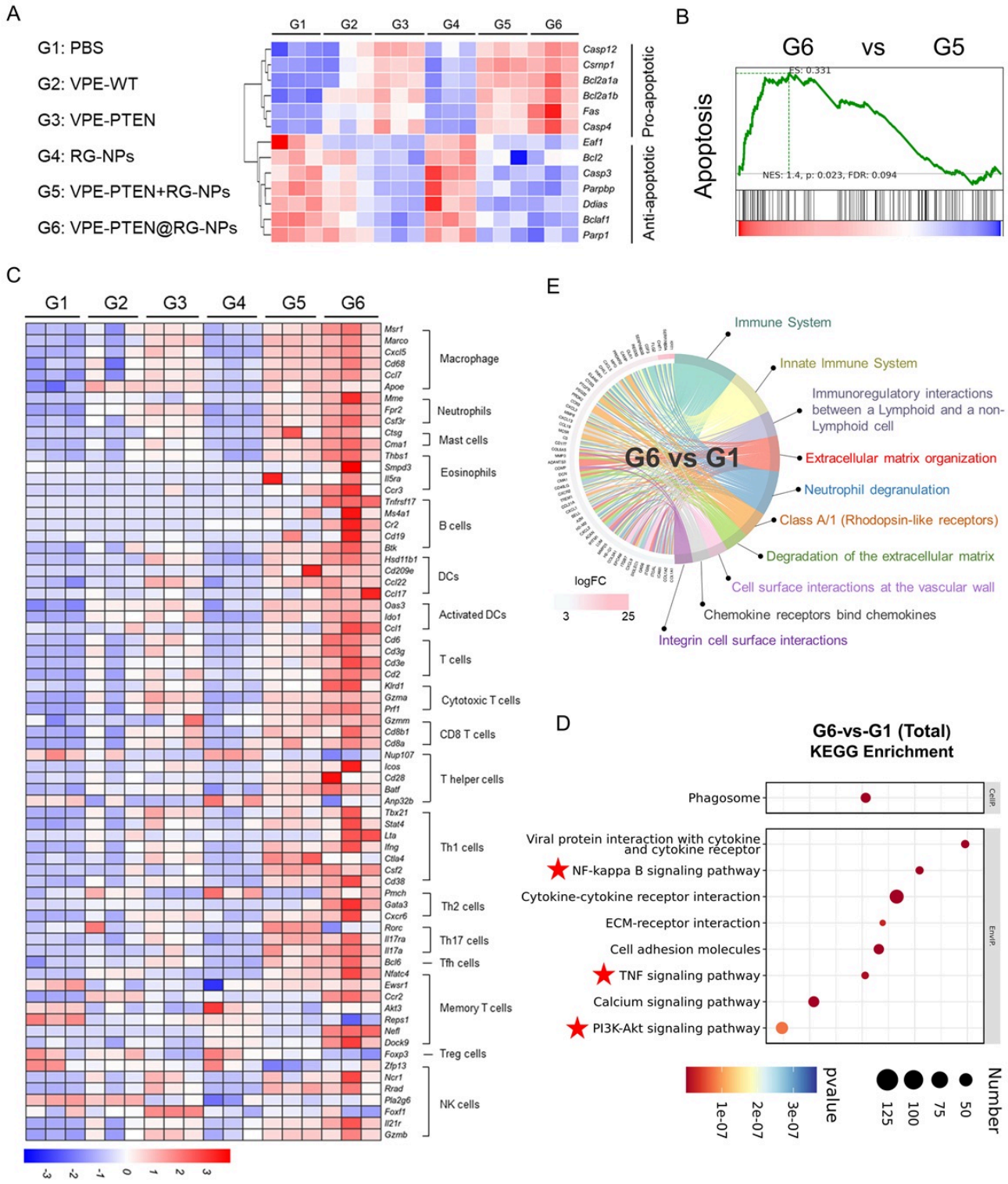


Figure 6

Transcriptomic analysis of tumor tissues. (**A**) Heatmap of genes associated with cell apoptosis. (**B**) Comparison of apoptosis-related signaling pathway changes between the VPE-PTEN+RG-NPs and VPE-PTEN@RG-NPs groups, analyzed by GSEA-based KEGG enrichment scores. (**C**) Heatmap of immune cell-associated gene expressions in different treatment groups. (**D**) KEGG pathway enrichment analysis of

differentially expressed genes between the PBS and VPE-PTEN@RG-NPs groups. (**E**) Reactome pathway enrichment analysis of differentially expressed genes between the PBS and VPE-PTEN@RG-NPs groups.

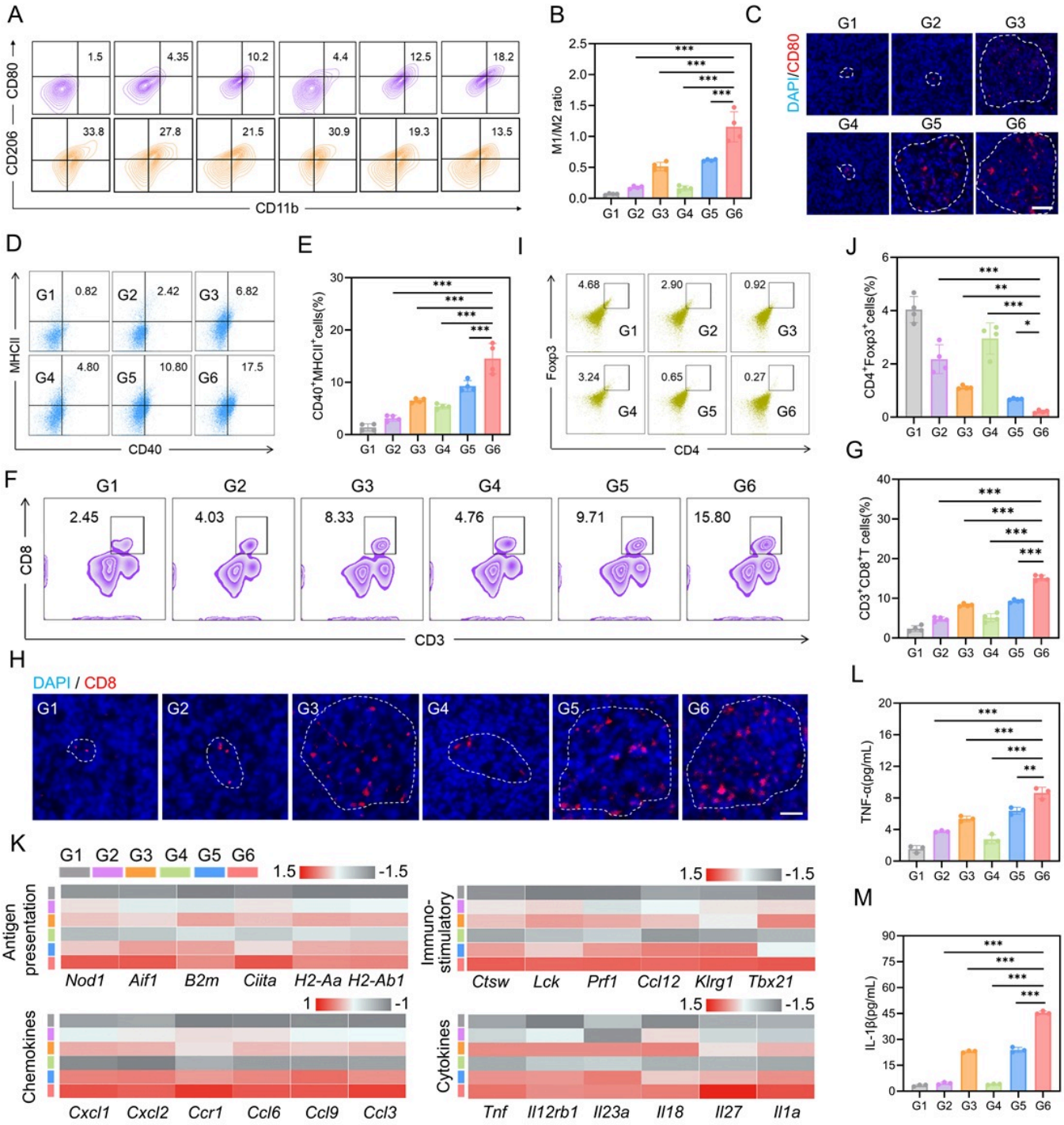


Figure 7

In vivo antitumor immune responses induced by VPE-PTEN@RG-NPs. (**A**) Representative flow cytometry plots of tumor-associated macrophage phenotypes, with M1 macrophages defined as

$CD11b^+CD86^+$ and M2 macrophages as $CD11b^+CD206^+$, in tumor tissues from different treatment groups. (**B**) Quantification of the M1-to-M2 macrophage ratio in different treatment groups. (**C**) Representative immunofluorescence images of M1-type macrophages in tumor tissues. Scale bar, 150 μm. (**D**) Representative flow cytometry plots and (**E**) quantification of tumor-infiltrating DCs in different treatment groups. (**F**) Representative flow cytometry plots of cytotoxic T lymphocytes ($CD3^+CD8^+$) in tumors and (**G**) their quantitative analysis. (**H**) Representative immunofluorescence images of $CD8^+$ T cells in tumor tissues. Scale bar, 150 μm. (**I**) Representative flow cytometry plots of Treg cells ($CD4^+Foxp3^+$) in tumor tissues after different treatments and (**J**) their quantitative analysis. (**K**) Heatmap analysis of gene expressions associated with antigen presentation, immunostimulatory chemokines, and cytokines in tumor tissues by RNA-sequencing data. (**L-M)** Levels of proinflammatory cytokines, including TNF-α (**L**) and IL-1β (**M**), in tumor tissues measured by ELISA. Data are presented as mean ± s.d. (n = 4). Statistical analysis was performed using one-way ANOVA. **P* < 0.05, ***P* < 0.01, ****P* < 0.001.

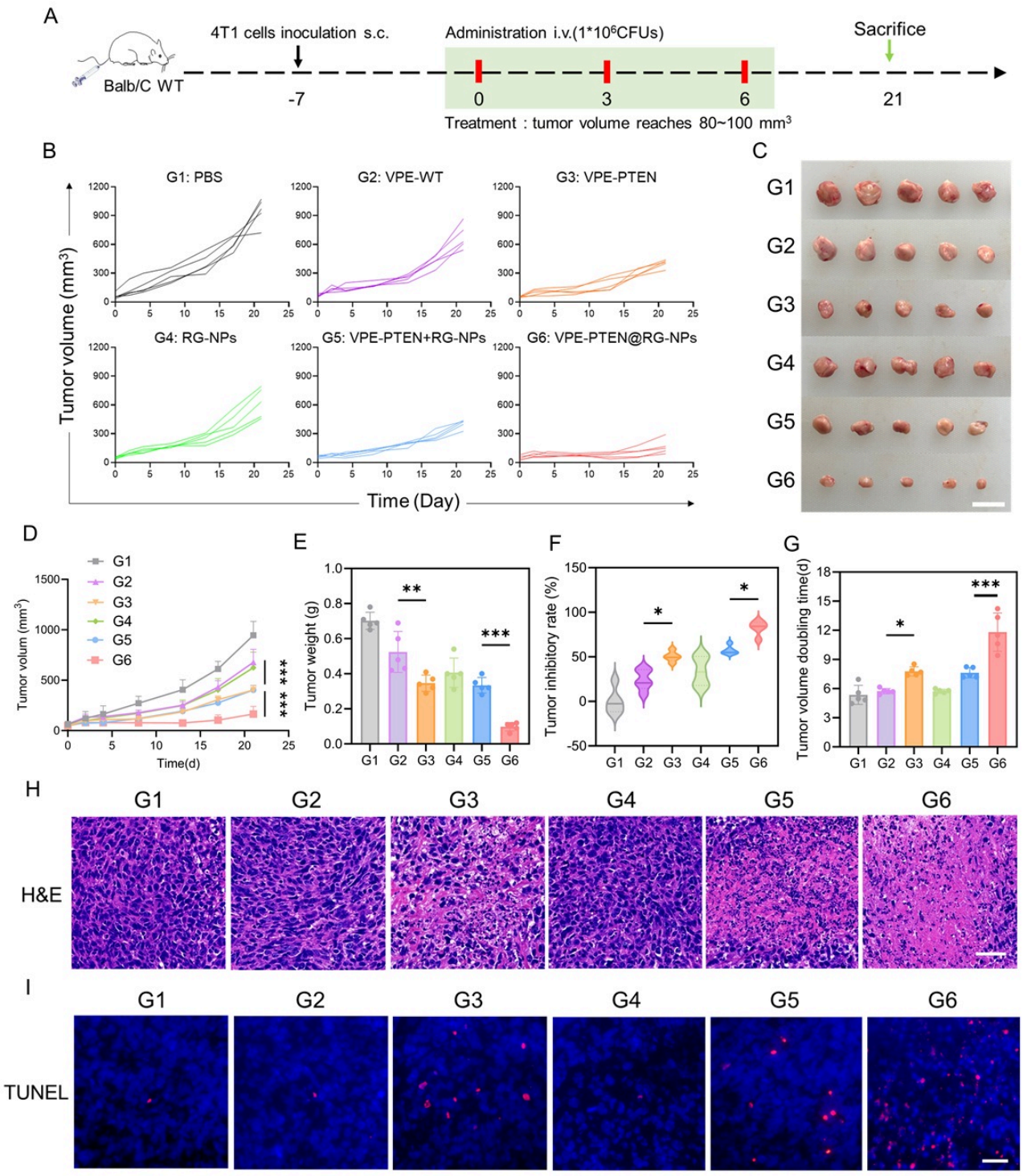


Figure 8

Antitumor efficacy of VPE-PTEN@RG-NPs in a murine 4T1 breast cancer model. (**A**) Schematic timeline for tumor establishment and treatment in the 4T1 tumor-bearing mouse model. (**B**) Tumor growth curves for the different treatment groups. (**C**) Representative images of excised tumors. Scale bar, 20 mm. (**D**) Tumor growth profiles after different treatments. (**E**) Tumor weights in different treatment groups. (**F**) Tumor inhibition rate and (**G**) tumor volume doubling time after different treatments. (**H**) Representative

H&E-stained tumor sections from different treatment groups. Scale bar, 150 μm. (**I**) Representative TUNEL staining images of tumor tissues indicating apoptotic cells. Scale bar, 50 μm. Data are presented as mean ± s.d. (n = 5). Statistical analysis was performed using one-way ANOVA (E, F, and G) or two-way ANOVA (**D**). *P < 0.05, **P < 0.01, ***P < 0.001.

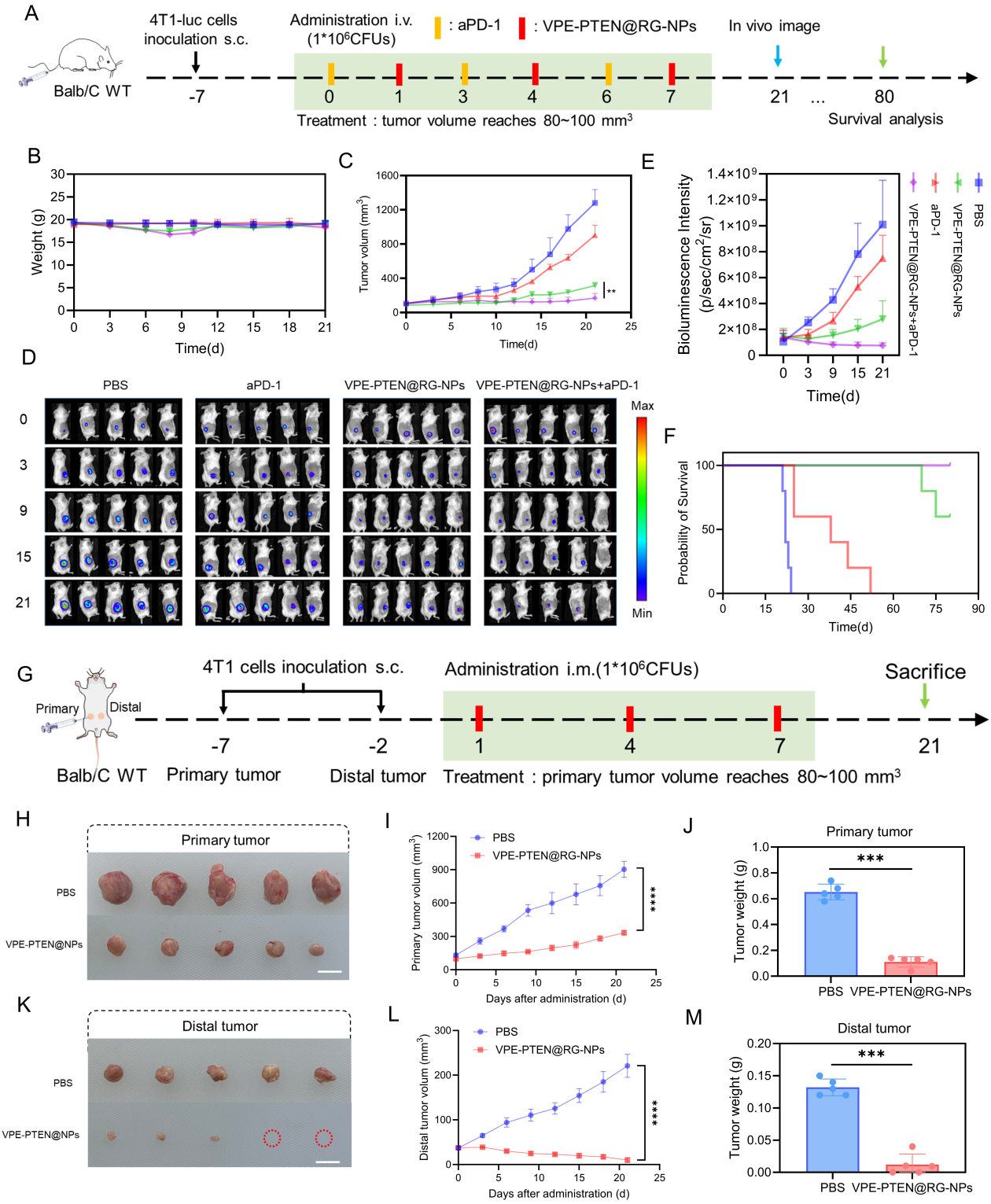


Figure 9

Therapeutic efficacy of VPE-PTEN@RG-NPs in combination with anti-PD-1 therapy. (**A**) Schematic timeline of the establishment and treatment of the 4T1-luc tumor-bearing mouse model. (**B**) Body weight changes of mice during the treatment period. (**C**) Tumor growth curves for the different treatment groups. (**D**) Representative in vivo bioluminescence images of mice bearing 4T1-luc tumors. (**E**) Quantification of tumor bioluminescence intensity based on region-of-interest analysis. (**F**) Survival curves of mice following different treatments. (**G**) Schematic illustration of the establishment and treatment strategy of the 4T1 double tumor model. (**H**) Representative images of excised primary tumors. (**I**) Growth curves of primary tumors. (**J**) Average primary tumor weights. (**K**) Representative images of excised distal tumors, with corresponding (**L**) growth curves and (**M**) average tumor weights. Scale bar, 10 mm. Data are presented as mean ± s.d. (n = 5). Statistical analysis was performed using one-way ANOVA (**J** and M) or two-way ANOVA (**C, E, I, and L**). $^{**}P < 0.01$, $^{***}P < 0.001$.

Supplementary Files

This is a list of supplementary files associated with this preprint. Click to download.

- SupportingInformation.docx
- Scheme1.docx